

## VISCOSITY &amp; ROTATION IN CORE-COLLAPSE SUPERNOVAE

TODD A. THOMPSON<sup>1,2</sup>, ELIOT QUATAERT<sup>3</sup>, & ADAM BURROWS<sup>4</sup>  
SUBMITTED TO APJ: *March 8, 2004*

## ABSTRACT

We construct models of core-collapse supernovae in one spatial dimension, including rotation, angular momentum transport, and viscous dissipation employing an  $\alpha$ -prescription. We compare the evolution of a fiducial  $11 M_{\odot}$  non-rotating progenitor with its evolution including a wide range of imposed initial rotation profiles ( $1.25 < P_0 < 8$  s, where  $P_0$  is the initial, approximately solid-body, rotation period of the iron core). This range of  $P_0$  covers the region of parameter space from where rotation begins to modify the dynamics ( $P_0 \sim 8$  s) to where angular velocities at collapse approach Keplerian ( $P_0 \sim 1$  s). Assuming strict angular momentum conservation, all models in this range leave behind neutron stars with spin periods  $\lesssim 10$  ms, shorter than those of most radio pulsars, but similar to those expected theoretically for magnetars at birth.

A fraction of the gravitational binding energy of collapse is stored in the free energy of differential rotation. This energy source may be tapped by viscous processes, providing a mechanism for energy deposition that is not strongly coupled to the mass accretion rate through the stalled supernova shock. This effect yields qualitatively new dynamics in models of supernovae. We explore several potential mechanisms for viscosity in the core-collapse environment: neutrino viscosity, turbulent viscosity caused by the magnetorotational instability (MRI), and turbulent viscosity by entropy- and composition-gradient-driven convection. We argue that the MRI is the most effective. We find that for rotation periods in the range  $P_0 \lesssim 3$  s, and a range of viscous stresses, that the post-bounce dynamics is significantly effected by the inclusion of this extra energy deposition mechanism; in several cases we obtain strong supernova explosions.

*Subject headings:* stars: magnetic fields — stars: neutron — supernovae: general — hydromagnetics

## 1. INTRODUCTION

Employing the now-standard suite of microphysics and a full solution to the Boltzmann equation for all neutrino species, the neutrino mechanism of core-collapse supernovae fails in one spatial dimension (Rampp & Janka 2000, 2002; Liebendörfer et al. 2001a,b; Mezzacappa et al. 2001; Thompson et al. 2003; Liebendörfer et al. 2004). The initial "bounce shock," formed as the core density reaches  $\sim 2 \times 10^{14}$  g cm<sup>-3</sup> and nuclei undergo a phase transition to free nucleons, stalls almost immediately due to a combination of neutrino losses, the ram pressure of the infalling mantle, and the dissociation of nuclei into neutrons and protons behind the shock. The revival of the shock to an asymptotic energy of order  $10^{51}$  erg is the focus of modern supernova theory. Any mechanism for this revival must fundamentally rely on the transfer of gravitational binding energy to the post-shock mantle. As its name makes clear, the "neutrino mechanism" (Bethe & Wilson 1985) relies on neutrino interactions (primarily  $\nu_e n \leftrightarrow p e^-$  and  $\bar{\nu}_e p \leftrightarrow n e^+$ ) to transfer binding energy to the shocked matter in the post-bounce epoch. In spherical models, the stalled bounce shock remains trapped forever and continues to accrete the overlying progenitor. Although some models show that multi-dimensional effects might be necessary for success of the neutrino mechanism (Herant et al. 1994; Burrows et al. 1995; Janka & Müller 1995, 1996; Fryer et al. 1999; Fryer & Warren 2002), multi-dimensional models employing more sophisticated neutrino transport fail to explode (Janka et al. 2002; Buras et al. 2003) — albeit marginally.

<sup>1</sup> Hubble Fellow<sup>2</sup> Astronomy Department & Theoretical Astrophysics Center, 601 Campbell Hall, The University of California, Berkeley, CA 94720; thomp@astro.berkeley.edu<sup>3</sup> Astronomy Department & Theoretical Astrophysics Center, 601 Campbell Hall, The University of California, Berkeley, CA 94720; eliot@astro.berkeley.edu<sup>4</sup> Steward Observatory, The University of Arizona, Tucson, AZ 85721; burrows@as.arizona.edu

In constructing one-dimensional models, the focus of the supernova community has been largely on refining details of the neutrino mechanism. These details include a fuller description of the nuclear physics and the neutrino interactions and, over the last ten years, a precise handling of neutrino transport (Mezzacappa & Bruenn 1993a,b,c; Burrows et al. 2000; Rampp & Janka 2000, 2002; Liebendörfer et al. 2001a,b; Mezzacappa et al. 2001; Thompson et al. 2003). Precision neutrino transport is important because the degree of neutrino heating behind the shock controls the subsequent dynamics and because the optical depth of this region is  $\lesssim 0.1$ . For this reason, the most recent one-dimensional models are fully spectral and multi-angle (Rampp & Janka 2000, 2002; Liebendörfer et al. 2001a,b; Mezzacappa et al. 2001; Thompson et al. 2003); neutrino transport also presents the most significant technical hurdle in calculating realistic models of core collapse in two or three spatial dimensions (Livne et al. 2003).

It is possible that yet more refined treatments of the radiation hydrodynamics or subtle changes in the microphysics of neutrino interactions may yield explosions in one-dimensional models via the neutrino mechanism. However, it is also possible that the solution to the supernova problem does not lie in such technical improvements or in an accumulation of five and ten percent effects, but instead in new physics and order unity phenomena not previously identified or fleshed out. Such improvements might include new massive pre-collapse progenitors with very different core entropy and lepton fraction, new

finite temperature high-density nuclear equations of state (including exotic meson species, quark matter, phase transitions, etc. and the associated neutrino microphysics), or the interplay between rotation and magnetic fields. In this paper, we take a step towards addressing the last of these issues in detail.

When the core of a rotating massive star collapses, some of the gravitational binding energy of collapse is stored in a strong shear profile. This free energy reservoir may be tapped by viscous processes. In this way, the binding energy of collapse, temporarily trapped in differential rotation, may be transferred to the matter as thermal energy. This is qualitatively different from the standard neutrino mechanism, which relies solely on neutrino interactions to communicate the binding energy of the collapsed iron core to the rest of the star. We find that dissipation of shear energy can significantly effect the dynamics of supernovae; models that would otherwise fail succeed as a result of viscous dissipation. The most promising source of viscosity is magnetic stresses generated by the magnetorotational instability (MRI) and perhaps magneto-convection (Duncan & Thompson 1992; Thompson & Duncan 1993). Although magnetic fields in excess of  $10^{15}$  G are generated by the MRI, no large iron core seed field is required for the success of this mechanism, since any seed field grows exponentially on a rotation period.

In §2, we provide some context and motivation for the present study and we review some previous research on core collapse with rotation. In §3, we describe the technical specifications of our one-dimensional models including rotation, viscous dissipation of shear energy, and the corresponding transport of angular momentum. Section 4 describes mechanisms for viscosity, including neutrino interactions, the MRI, and hydrodynamic convection. In §5, we present results from rotating models of core collapse including the centrifugal force, but without viscous dissipation. We also provide a general discussion of the conditions for explosion and an explanation for why these models and non-rotating models fail. We compare the magnitude of the viscous processes discussed in §4 in §6. In §7, we present results from calculations of core collapse including viscous dissipation. We show that explosions are obtained, we explain why these models succeed, and we delineate the successful parameter space. In §8, we summarize our results and discuss the implications of our findings.

## 2. SCENARIO & MOTIVATION

When the iron core of a massive star collapses as a result of the Chandrasekhar instability, the implosion is reversed at nuclear densities. Here, nuclei dissociate into free nucleons and the equation of state stiffens dramatically, driving the bounce shock wave into the supersonic infalling outer core. The bounce shock stalls almost immediately and a characteristic post-bounce quasi-steady-state accretion structure is obtained. The hot (temperatures of order 10 MeV) newly-born protoneutron star (PNS) has a neutrinosphere radius,  $R_\nu$ , of approximately 50 – 80 km (defined here by the radius at which the optical depth to electron neutrinos  $\sim 2/3$ , a very energy-dependent quantity). Overlying the PNS is a subsonic accretion flow, bounded by the stalled stand-off bounce shock at a radius of  $\sim 150$  – 200 km. The region between the PNS and the shock consists of a cooling layer just above the PNS and a region of net heating (the "gain" region) between the cooling layer and the shock. The boundary between net cooling and net heating is called the gain radius,  $R_g$ , typically at  $\sim 100$  km. Neutrino heating is provided by both accretion luminosity as the matter

falling through the bounce shock is incorporated into the PNS and core neutrino luminosity as the PNS cools and deleptonizes.

During collapse, the inner parts of the iron core collapse to smaller radii than the outer parts. Thus, if one begins with a solid-body rotation profile at the moment the core becomes unstable, as the collapse proceeds, strong differential rotation – a negative shear ( $d\Omega/d\ln r$ , where  $\Omega$  is the angular velocity and  $r$  is the radial coordinate) profile – naturally develops (LeBlanc & Wilson 1970; Fryer & Heger 2000; Akiyama et al. 2003; Ott et al. 2003). The strong shear profile created during collapse persists as the shock is formed, as it stalls, and as the accretion phase begins. The shear continues to grow, particularly at the PNS surface, as material is advected inward and the whole progenitor core is accreted. This shear profile is a reservoir of free energy, a portion of the gravitational binding energy of collapse trapped as differential rotation.

Heger et al. (2000) have computed the evolution of rotating stars with zero-age-main sequence masses greater than  $10 M_\odot$  and with initial equatorial surface angular velocities up to approximately 70% of breakup. Although spherical, these models account for angular momentum transport via a variety of instabilities and include the effects of the centrifugal force up to central neon burning. Heger et al. (2000) neglect rotational effects in the momentum equation and energy equation during the evolution from neon burning to core collapse. The specific angular momentum they predict in the roughly solid-body iron core that forms prior to core collapse is  $j \sim 10^{16} – 10^{17} \text{ cm}^2 \text{ s}^{-1}$ , with central angular velocities  $\sim 1 – 10 \text{ rad s}^{-1}$ . On collapse, the PNS is formed with a mass  $\sim 1.2 M_\odot$  and a radius of  $\sim 8 \times 10^6 \text{ cm}$ . The ratio of pre-collapse to post-collapse radius for a mass element which comprises the PNS is typically 10 – 20, implying, via angular momentum conservation, an increase in the ratio of pre-collapse to post-collapse angular velocity of 100 – 400. Taking intermediate values for the initial angular velocity of the iron core, the total energy in shear can then be estimated:

$$E_{\text{Shear}} \sim 10^{52} \text{ erg} \left( \frac{M_{\text{PNS}}}{1 M_\odot} \right) \left( \frac{R_\nu}{50 \text{ km}} \right)^2 \left( \frac{\Omega}{10^3 \text{ rad s}^{-1}} \right)^2, \quad (1)$$

corresponding to a spin period near the PNS surface of  $\sim 6 \text{ ms}$ . The total energy in shear in the gain region, exterior to the PNS, may be less by an order of magnitude, but is replenished on a freefall timescale as more of the progenitor falls through the standoff supernova shock. Although shear energy in the range of  $10^{51} – 10^{52} \text{ erg}$  is small on the scale of the binding energy of the resulting fully contracted neutron star and the energy liberated in neutrinos, it is large on the scale of the canonical asymptotic supernova energy and (not coincidentally) the binding energy of the matter exterior to the gain radius,  $\sim 10^{51} \text{ erg}$ . If this free energy source can be tapped on a timescale comparable to, for example, the neutrino heating timescale in the gain region, we expect large modifications to the dynamics.

Any local viscous process acting in a region of differential rotation will transport angular momentum and dissipate the energy stored in shear on a viscous timescale. It is this mechanism for transferring gravitational binding energy, stored during collapse as shear energy, to the matter in the gain region that we explore in this paper. To this end, we consider several potential mechanisms for viscosity: microscopic shear neutrino viscosity and the turbulent viscosity caused by convective or magnetic stresses. Generation of these turbulent stresses is caused by unstable entropy, composition, or angular velocity gradients. As an expedient, we distinguish between magnetic stresses caused by the magnetorotational instability (MRI) and

the turbulent viscosity of purely hydrodynamical convection (see §4.2 and §4.3). We compare these agents of viscosity and find that the MRI and hydrodynamical convection dominate microscopic neutrino viscosity and that the latter is likely not capable of modifying the dynamics of supernovae. We find that for fast enough initial rotation periods, dissipation of shear energy can effect the subsequent dynamics significantly; a stalled shock can be revived and driven to infinity; a dud is transformed into an explosion. We emphasize that for the success of this mechanism we do not require large seed magnetic fields in the iron core prior to collapse. The large magnetic fields generated from even a vanishingly small initial field are a necessary consequence of the MRI in rapidly rotating collapse (Akiyama et al. 2003).

The calculations presented in this paper are one-dimensional. Spherical symmetry is assumed here, but demonstrably broken in a rotating system. We have attempted to partially mitigate this issue by restricting our calculations to those in which, throughout the evolution, Keplerian rotational velocities are not attained. That is, for every model presented, at every time and at all radii,  $\Omega(r) < \Omega_K = \sqrt{GM/r^3}$ . By imposing this restriction, the momentum equation is dominated by the gradients in the thermal pressure and the gravitational force; we calculate stars, not disks. That said, for  $E_{\text{shear}}$  to be in an interesting energy range (say  $\gtrsim 10^{50}$  erg) rotation rates for the iron core at collapse must be in the range of a few  $\text{rad s}^{-1}$ . Assuming strict conservation of angular momentum and that the supernova leaves behind a  $\sim 1.4 M_{\odot}$  neutron star with a radius of  $\sim 10$  km, we find that this energy requirement implies an initial spin period for the young neutron star of at most  $\sim 10$  milliseconds. Observations of radio pulsars imply that the initial rotation rate of neutron stars should be in the range of many tens to hundreds of milliseconds (e.g. Kaspi & Helfand 2002), factors of hundreds to tens of thousands lower in rotational energy. Thus, although we restrict ourselves to models that are slowly rotating on the scale of  $\Omega_K$ , they are rapidly rotating on the scale of observed neutron stars. However, caution is warranted in taking this argument too seriously. Gravitational radiation (e.g. Ostriker & Gunn 1969), magnetic dipole radiation (e.g. Pacini 1967, 1968; Gunn & Ostriker 1969; Lindblom et al. 2001; Arras et al. 2003), magneto-centrifugal winds (Thompson 2003; Thompson, Chang, & Quataert 2004), and late-time fallback (see Woosley & Heger 2003 and references therein) can spindown young neutron stars, complicating the inference of "initial" neutron star spin periods (Kaspi & Helfand 2002). Nevertheless, it is possible that rapid rotation is relevant in only a subset of all core-collapse supernovae (e.g. those producing magnetars; Duncan & Thompson 1992; Thompson & Duncan 1993). The size of that subset is unknown.

In addition to the various processes that may slow a neutron star at or just after birth, it is also possible that stellar evolution produces slowly rotating iron cores. Recent models of Heger et al. (2003) based on the work of Spruit (2002, 2003) attempt to evolve core-collapse progenitors including angular momentum transport via magnetic processes. These effects yield significantly smaller iron core specific angular momenta ( $j \sim 10^{14} - 10^{15} \text{ cm}^2 \text{ s}^{-1}$ ,  $\Omega \lesssim 0.1 \text{ rad s}^{-1}$ ), implying much lower shear energy. Even smaller rotation periods were found in Spruit & Phinney (1998). Hence, uncertainty in models of rotational stellar evolution remains high.

Similar uncertainty surrounds models of rotating core collapse and the role of rotation and magnetic fields in the mech-

anism of supernovae. Although pioneering, the MHD calculation of rotational core-collapse by Leblanc & Wilson (1970) is now largely obsolete because the neutrino microphysics, nuclear equation of state, and progenitor configuration they employed have been superseded. The jet-like explosion their calculation produced was reconsidered with more modern input physics by Symbalisty (1984), who showed that only with initial iron core spin periods much less than one second and a very large fossil seed field in the progenitor iron core, could jet-driven explosions be obtained.

The recent work of Akiyama et al. (2003) considered the potential effects of the MRI in stellar collapse. They showed that much of the post-bounce core collapse environment is unstable to the MRI and that large saturation magnetic fields are naturally produced. Energy deposition via local turbulent dissipation was neglected in their study. Instead, Akiyama et al. (2003) argued that the very large field strengths generated by the MRI create a jet with sufficient MHD luminosity to explode the star as in the models of Khokhlov et al. (1999). This argument assumes that the magnetic field generated by the MRI can form the organized large-scale fields required for collimation and jet formation. A limitation of the models presented by Akiyama et al. (2003) is that they were not self-consistent. They did not include rotation in the dynamics and because they neglected angular momentum transport, the energy available for the MHD jets they consider may have been overestimated.

Fryer & Heger (2000) considered rotating core-collapse in two spatial dimensions, and recently Fryer & Warren (2004) extended these rotating models to three dimensions. The only effect of rotation on the explosion mechanism that Fryer & Heger (2000) and Fryer & Warren (2004) discuss is the suppression of convection in the equatorial plane due to the stabilizing centrifugal force. However, for stabilization to occur, rotation must be important enough that if the calculation had been performed in MHD the equatorial region would have been destabilized by the MRI. Thus, the stabilization that occurred in their hydrodynamic calculations is somewhat artificial and it is a signal that the simulations must be performed in MHD. All models computed in Fryer & Heger (2000) and Fryer & Warren (2004) explode. For this reason, Fryer & Heger (2000) and Fryer & Warren (2004) did not assess the role of viscous heating, the competition between different possible sources of viscosity, or the potential role of rotation itself in generating explosions. Finally, Fryer & Warren (2004) concluded that the saturation magnetic field strength throughout the post-collapse structure is orders of magnitude lower than the field estimated in Akiyama et al. (2003). We address this conclusion in §5 and find that large fields in the range  $10^{14} - 10^{16}$  G can be typical in rotating core collapse (Duncan & Thompson 1992; Thompson & Duncan 1993; in agreement with Akiyama et al. 2003).

### 3. THE MODEL

The core-collapse supernova code we have developed and that we employ here, SESAME<sup>5</sup>, is described in detail in Burrows et al. (2000) and Thompson et al. (2003). The hydrodynamics scheme is Lagrangean, Newtonian, explicit, and employs artificial viscosity for shock resolution. The radiation transport algorithm solves the order  $V/c$  Boltzmann equation (Eastman & Pinto 1993) for three neutrino species:  $\nu_e$ ,  $\bar{\nu}_e$ , and " $\nu_{\mu}$ ", employing the standard approximation that the non-electron neutrino species can be treated collectively. It

<sup>5</sup> Spherical Explicit/Implicit Supernova Algorithm for Multi-Group/Multi-Angle Explosion Simulations.

is fully spectral, employs the tangent-ray technique for angular discretization of the radiation field, and is based on the Feautrier variables. The neutrino physics employed is standard and described in Bruenn (1985), Thompson (2002), Burrows & Thompson (2002), and Thompson et al. (2003). Notable additions include nucleon-nucleon bremsstrahlung (Burrows et al. 2000; Thompson et al. 2000), and weak-magnetism and recoil corrections to both the charged-current neutrino-nucleon absorption/emission processes and elastic neutrino-nucleon scattering (Horowitz 1997; Horowitz 2002). Inelastic neutrino-electron/positron scattering is calculated with a fast and accurate explicit scheme described in Thompson et al. (2003). The equations of radiation hydrodynamics are coupled to an efficient tabular version of the Lattimer-Swesty high-density nuclear equation of state (for  $\rho \gtrsim 10^7 \text{ g cm}^{-3}$ ) and the Helmholtz equation of state (for  $\rho \lesssim 10^7 \text{ g cm}^{-3}$ ; Timmes & Arnett 1999; Timmes & Swesty 2000; Thompson et al. 2003). All of the models presented here are calculated with 20 energy groups per neutrino species and 500 Lagrangean mass zones.

### 3.1. Additions to the Standard Algorithm

To the standard set of Newtonian equations for Lagrangean hydrodynamics in one spatial dimension, we add rotation via the term  $f_\theta j^2/r^3$  in the momentum equation, where  $j$  is the specific angular momentum,  $r$  is the radial coordinate, and  $f_\theta (=2/3)$  results from taking the angular average for one dimensional parameterizations of rotation (Heger et al. 2000).

Angular momentum transport is calculated by solving the equation

$$\frac{Dj}{Dt} = \frac{1}{\rho r^2} \frac{d}{dr} \left( \xi \rho r^4 \frac{d\Omega}{dr} \right), \quad (2)$$

where  $D/Dt = \partial/\partial t + \mathbf{V} \cdot \nabla$ ,  $\rho$  is the mass density,  $\Omega$  is the angular velocity, and  $\xi$  is the shear viscosity.<sup>6</sup> Equation (2) is solved explicitly in operator-split fashion from the rest of the radiation-hydrodynamical algorithm. During a given calculation, depending on the magnitude of the viscosity, the diffusive timestep ( $\Delta t < \min[(\Delta r)^2/2\xi]$ ) becomes shorter than the Courant-limited hydrodynamical timestep and we sub-cycle the calculation of the update to  $j$ .

The dissipation of shear energy is handled by adding a term to our Lagrangean equation for the specific internal energy ( $e$ );

$$\frac{De}{Dt} = [\dots] + \xi \left( \frac{d\Omega}{d\ln r} \right)^2, \quad (3)$$

where the actual form of  $\xi$  and the resulting viscous energy deposition rate ( $\dot{q}_\xi$ ) depends on the specific viscous process considered. Note that we dissipate shear energy locally. For a source of microscopic viscosity this is appropriate. However, for a turbulent viscosity like the MRI, it may be that energy stored in the turbulent magnetic field can be transported and deposited non-locally. This would relieve the requirement in the models presented here that a region of high local viscous dissipation must correspond to a region of large shear. However, a multi-dimensional MHD treatment is required to address this question fully in the supernova context.

### 3.2. The Progenitors

We consider two progenitors. The first is the non-rotating  $11 \text{ M}_\odot$  progenitor of Woosley & Weaver (1995). This model is

<sup>6</sup> Our use of " $\xi$ " to denote "viscosity" alleviates confusion with " $\nu$ ", which we use to denote neutrinos or neutrino quantities.

zoned out to  $1.45 \text{ M}_\odot$ , corresponding to a radius of  $\sim 4000 \text{ km}$ . We impose rotation on the core of the progenitor, taking

$$\Omega(r) = \frac{\Omega_0}{1 + (r/R_\Omega)^2}, \quad (4)$$

where  $r$  is the spherical radial coordinate and not the cylindrical radial coordinate. Equation (4) implies that the rotation profile is roughly solid-body out to  $R_\Omega$ . Comparing with the rotating stellar progenitors of Heger et al. (2000), eq. (4) provides a reasonable approximation to  $\Omega(r)$  with  $R_\Omega$  near  $\sim 1000 \text{ km}$ . Our models span spin periods in the range  $1 \lesssim P_0 \lesssim 10 \text{ seconds}$  ( $P_0 = 2\pi/\Omega_0$ ). As discussed in §2, we restrict ourselves to models in which  $\Omega(r) < \Omega_K$  at all times and at all radii during a given calculation. For our  $11 \text{ M}_\odot$  model and for  $\Omega(r)$  set by eq. (4) with  $R_\Omega = 1000 \text{ km}$ , we find that  $P_0 \geq 1.25 \text{ s}$  satisfies this constraint. This sets our lower bound on  $P_0$ . The upper bound on  $P_0$  is set by the fact that our spherical models with  $P_0 > 8 \text{ s}$  and  $R_\Omega = 1000 \text{ km}$  are nearly indistinguishable from models with  $P_0 = \infty$ . In all models with this  $11 \text{ M}_\odot$  progenitor we take  $R_\Omega = 1000 \text{ km}$ .

The second progenitor we consider is the rotating  $15 \text{ M}_\odot$  model E15A of Heger et al. (2000), which we zone out to an enclosed mass of  $1.65 \text{ M}_\odot$ . With this model we can compare directly to the 2D axisymmetric core-collapse calculations of Fryer & Heger (2000) and the 3D calculations of Fryer & Warren (2004).

Figure 1 shows  $\Omega(r)$  for the progenitor models considered here. Solid lines are for the  $11 \text{ M}_\odot$  progenitor with  $P_0 = 1.25, 2, 3, 4, 5$ , and  $8 \text{ seconds}$ . The dashed line shows  $\Omega(r)$  for the  $15 \text{ M}_\odot$  model from Heger et al. (2000). Throughout this paper we use "E15A" to refer to the  $15 \text{ M}_\odot$  progenitor of Heger et al. (2000) and " $P_0 =$ " in referring to the  $11 \text{ M}_\odot$  models.

## 4. VISCOSITY

In this section, we discuss the pure microscopic shear viscosity caused by neutrinos and two forms of turbulent viscosity: the magnetorotational instability and hydrodynamic convection. We compare the magnitude of these viscous processes in §6 in the context of the rotating models of core collapse presented in §5. In §7, our results for rotating models including viscous dissipation are discussed.

### 4.1. Neutrino Viscosity

When neutrinos are fully diffusive, the shear viscosity is given by (van den Horn & van Weert 1984; Burrows & Lattimer 1988; Thompson & Duncan 1993)

$$\xi_\nu = \frac{4}{15} \frac{E_\nu}{\rho c} \langle \lambda_\nu \rangle, \quad (5)$$

where  $E_\nu$  is the neutrino energy density,  $\langle \lambda_\nu \rangle$  is the average neutrino mean-free path,

$$\langle \lambda_\nu \rangle = \left\{ \int d\varepsilon_\nu \varepsilon_\nu^2 \lambda_\nu(\varepsilon_\nu) \tilde{J}_\nu(\varepsilon_\nu) \right\} / \left\{ \int d\varepsilon_\nu \varepsilon_\nu^2 \tilde{J}_\nu(\varepsilon_\nu) \right\}, \quad (6)$$

$$\tilde{J}_\nu(\varepsilon_\nu) = \frac{1}{2} \int_{-1}^1 d\mu f_\nu(\mu, \varepsilon_\nu), \quad (7)$$

$f_\nu$  is the invariant neutrino phase-space distribution function,  $\varepsilon_\nu$  is the neutrino energy, and  $\mu = \cos\theta$ .

Such a prescription for the viscous effects of neutrinos applies only in the region of diffusive neutrino transport, below the neutrinospheres, where  $\langle \lambda_\nu \rangle \ll r$ . In the optically thin region, as  $\langle \lambda_\nu \rangle \rightarrow \infty$ , eq. (5) is inapplicable. Nearest the neutrinospheres,  $\xi_\nu$  will be large, but outside this region the viscosity is not well defined. However, the effect of the streaming neutrinos interacting with the background differential rotation profile and the distribution of hydrodynamic (convective) and magnetohydrodynamic (magneto-convective) fluctuations can still be quantified. Neutrinos propagating through the cooling and gain regions damp fluctuations with a characteristic rate (Jedamzik et al. 1998; Agol & Krolik 1998)

$$\Gamma_\nu \sim \frac{E_\nu}{\langle \lambda_\nu \rangle \rho c}. \quad (8)$$

For example, if a convective mode of wave number  $k$  in the gain region has linear growth rate given  $\sqrt{|N^2|}$ , then if  $\Gamma_\nu > \sqrt{|N^2|}$  the convective mode will be damped. Similarly, if the MRI grows in the gain region on a timescale  $\sim \Omega^{-1}$ , if  $\Gamma_\nu > \Omega$  the linear MRI mode will also be damped.

#### 4.2. The Magnetorotational Instability

In the equatorial region, neglecting gradients in the  $\theta$ -direction<sup>7</sup>, the Solberg-Høiland condition for instability in the presence of rotation, but without magnetic fields is given by (Tassoul 1978)

$$N^2 + \kappa^2 < 0, \quad (9)$$

where  $\kappa$  is the epicyclic frequency,

$$\kappa^2 = 4\Omega^2 + \frac{d\Omega^2}{d\ln r}, \quad (10)$$

and  $N$  is the Brunt-Väisälä frequency. In the supernova context, material may be driven convectively unstable by negative gradients in entropy ( $s$ ) or in lepton number ( $Y_l$ ). For our purposes here, it is sufficient to replace  $Y_l$  with the electron fraction ( $Y_e$ ), thereby neglecting the electron neutrino fraction  $Y_{\nu_e}$  in regions where this species is trapped and diffusive. The expression for the Brunt-Väisälä frequency used in this paper is then (Lattimer & Mazurek 1981)

$$N^2 = \frac{g}{\gamma} \left( \frac{1}{P} \frac{\partial P}{\partial s} \bigg|_{\rho, Y_e} \frac{ds}{dr} + \frac{1}{P} \frac{\partial P}{\partial Y_e} \bigg|_{\rho, s} \frac{dY_e}{dr} \right), \quad (11)$$

where  $g$  is the effective gravity and  $\gamma = d\ln P/d\ln \rho|_s$ . When magnetic fields are included in the stability analysis of differentially rotating bodies, a "generalized" Solberg-Høiland criterion is obtained (Balbus & Hawley 1991; 1992a,b; 1994; 1998). The condition

$$N^2 + \frac{d\Omega^2}{d\ln r} < 0, \quad (12)$$

replaces eq. (9) as the criterion for instability in the equatorial region. Ignoring gradients in entropy and composition, a magnetized differentially rotating fluid is unstable to the magnetorotational instability if  $d\Omega^2/d\ln r < 0$ . The linear growth rate for the fastest growing mode is (Balbus & Hawley 1991)

$$\Gamma_{\text{MRI}} = \frac{1}{2} \left| \frac{d\Omega}{d\ln r} \right|. \quad (13)$$

<sup>7</sup> The Solberg-Høiland criterion for instability contains latitudinal gradients that for a star may be as large as those in the radial direction. For the purposes of the discussion here, and in the spirit of the one-dimensional calculations presented in this paper, we retain only the latter.

<sup>8</sup> Akiyama et al. (2003) estimate the MRI viscous timescale as  $\tau_{\text{visc}} \sim B_\phi \beta_M / (2B_r \Omega)$ , where  $\beta_M = P/(B^2/8\pi)$  (see their eq. 32). Because  $\beta_M \gg 1$  in a star, they neglect the redistribution of angular momentum by magnetic stresses. This is incorrect. In estimating the  $\alpha$  parameter, they take  $\alpha \sim B_r B_\phi / (4\pi P)$ , and it is in this way that  $\beta_M$  enters their  $\tau_{\text{visc}}$ . Their estimate for  $\alpha$ , however, is relevant for disks only. In the stellar context,  $\tau_{\text{visc}} \sim (\alpha \Omega)^{-1} (r/H)^2$ . For most of our models this estimate yields  $\tau_{\text{visc}} \sim 0.1$  s at  $R_\nu$  and  $\tau_{\text{visc}} \sim 1$  s at  $R_g$  and so angular momentum redistribution cannot be neglected.

To rough, but useful, approximation,  $\Gamma_{\text{MRI}} \sim \Omega$ . In a sub-sonic, steady-state accretion flow with net heating, as in the gain region just interior to the shock in the supernova context, the entropy gradient is negative, and compositional gradients are insufficient to stabilize this region. Because the process of collapse, along with angular momentum conservation implies negative shear in the gain region, eq. (12) implies that as long as  $\Gamma_\nu < \Gamma_{\text{MRI}}$  this region must be unstable to the MRI.

Our form for the viscosity due to the MRI is motivated by consideration of the Maxwell stress ( $t_{r\phi}$ ):

$$t_{r\phi} = B_r B_\phi / 4\pi \sim B^2 / 4\pi = V_A^2 \rho, \quad (14)$$

where  $V_A = B/\sqrt{4\pi\rho}$  is the Alfvén velocity. The viscous shear stress is given by  $\xi\rho|d\Omega/d\ln r| \sim \xi\rho\Omega$ . Equating the Maxwell stress and the shear stress we find that  $\xi_{\text{MRI}} \sim V_A^2/\Omega$ . For the MRI,  $V_A k \sim \Omega$  for the fastest growing mode of wave number  $k$ . Taking  $k \sim 1/H$ , where  $H$  is the pressure scale height, and substituting, we find that  $\xi_{\text{MRI}} \sim H^2\Omega$ , up to factors of  $d\ln\Omega/d\ln r$ . We introduce a constant of order unity, an  $\alpha$  parameter (typically 0.1), and take

$$\xi_{\text{MRI}} = \alpha H^2 \Omega. \quad (15)$$

Equation (15) is appropriate for the form of the viscous stress regardless of the ratio  $V_\phi/c_s$ .<sup>8</sup> In all models considered in this work,  $V_\phi$  is less than or much less than  $c_s$  and  $V_{\text{Kep}}$ . This condition emphasizes the fact that we consider stars, not disks. In accretion disks,  $H = c_s/\Omega$ . Substituting into eq. (15) one obtains the classic form for the shear stress in accretion disks from Shakura & Sunyaev (1973),  $\xi = \alpha c_s H$ . Another way to see that eq. (15) is the appropriate form for the viscosity is to recognize that any turbulent viscosity can be estimated as the product of a turbulent velocity ( $V_{\text{turb}}$ ) and a correlation length ( $L$ ) for fluctuations. In the case of a disk the adiabatic sound speed  $c_s$  is  $V_{\text{turb}}$  and  $L$  is the pressure scale height,  $H$ . In a star, with  $H\Omega$  less than or *much* less than  $c_s$ ,  $V_\phi = r\Omega$  takes the place of  $c_s$  as  $V_{\text{turb}}$ . The correlation length for the MRI remains the pressure scale height and eq. (15) follows.

Beginning with an arbitrarily small seed field, the MRI increases the magnetic field strength exponentially on a timescale  $\sim \Omega^{-1}$ . In models of accretion disks, the MRI in ideal MHD saturates such that the toroidal component of the Alfvén speed comes into rough equipartition with the sound speed. In the stellar context considered here, the Alfvén speed should saturate at or order the rotation speed,

$$B_{\text{Sat}_\phi} \sim (4\pi\rho)^{1/2} V_\phi. \quad (16)$$

The value of the toroidal saturation magnetic energy density ( $B_{\text{Sat}_\phi}^2/8\pi$ ) may be somewhat less (a factor of  $\sim 10$ ) than the value implied by eq. (16) (see, e.g., Hawley et al. 1996 and Stone et al. 1996 for results in the accretion context). A reduction of this magnitude in the energy density implies a rather small correction to the field strength  $B_{\text{Sat}_\phi}$ . Further possible corrections to eq. (16) are order unity and include factors of  $d\ln\Omega/d\ln r$  (Akiyama et al. 2003). The magnitude of the saturation energy density in the poloidal direction is roughly an order of magnitude smaller than  $B_{\text{Sat}_\phi}$  (e.g. Balbus & Hawley 1998).

### 4.3. Convective Viscosity

The Brunt-Väisälä frequency is always negative in the gain region. Convection, driven by neutrino heating, results (Herant et al. 1994; Burrows, Hayes, & Fryxell 1995; Janka & Müller 1996; Mezzacappa et al. 1998; Buras et al. 2003). If convection has time to develop fully, and the Reynolds number is high, the presence of turbulent convection may result in the dissipation of shear energy in much the same way as turbulence caused by the MRI. The convective viscosity ( $\xi_{\text{Con}}$ ) can be naively estimated as the product of the turbulent velocity (in this case the convective velocity  $V_{\text{Con}}$ ) and the correlation length:

$$\xi_{\text{Con}} \sim HV_{\text{Con}}/3. \quad (17)$$

The convective velocity can be estimated from mixing length theory:

$$V_{\text{Con}} = 2gl(\delta\rho/\rho), \quad (18)$$

where  $g = -\rho^{-1}dP/dr = P/\rho H$ ,  $l$  is the mixing length, and  $\delta\rho = (d\rho/dr - \Delta\rho/l)l$ . In the gain region,  $V_{\text{Con}}$  is typically  $\sim 5 \times 10^8 - 10^9 \text{ cm s}^{-1}$ . Unfortunately, this estimate is very rough because even the sign of the Reynolds stress, which dictates the direction of angular momentum transport in a convective region, is uncertain and may depend sensitively on the Rossby number, the ratio of the rotation period to the convective turnover time (Chan 2001; Käpylä, Korpi, & Tuominen 2003). In general, for Rossby numbers less than unity the Reynolds stress is positive and angular momentum transport is outward. However, this statement depends on latitude and the magnitude of the heat flux through the convection zone. In the supernova context, particularly for rotation rates with  $V_\phi \ll c_s$  in the gain region (and deep in the PNS interior), we expect the Rossby number to be greater than unity (Thompson & Duncan 1993).

It is not strictly correct to speak of two different mechanisms for turbulent convective viscosity; the MRI and hydrodynamical convection come together. There is just one turbulent stress tensor, containing Reynolds and Maxwell correlations, of the form  $\langle u_i u_\phi - u_{A_i} u_{A_\phi} \rangle$ , where  $u$  is the fluctuation velocity and  $u_{A_i} = B_i/\sqrt{4\pi\rho}$  is the fluctuation Alfvén speed in direction  $i$ ; and convection itself will, of course, amplify magnetic fields even in the absence of the MRI, thereby generating appreciable magnetic stresses (Duncan & Thompson 1992; Thompson & Duncan 1993). But one term in the stress tensor may dominate the other and for the purposes of this paper we distinguish between purely hydrodynamical convection ( $\Gamma_{\text{Con}} \gg \Gamma_{\text{MRI}}$ ) and the case where the Maxwell stress is comparable to or dominates the Reynolds stress (see Narayan et al. 2002 for a more general discussion).

## 5. CORE COLLAPSE WITH ROTATION, BUT WITHOUT VISCOUS DISSIPATION

In this section we describe results from a set of simulations with the  $11 M_\odot$  progenitor with  $P_0 = 1.25, 2, 3, 4, 5$ , and 8 seconds as well as results with model E15A from Heger et al. (2000) (see §3.2). In these models we include the centrifugal force, but neglect diffusive angular momentum transport. We do this in order to separate the effects of the centrifugal force from the effects of viscous dissipation. Table 1 summarizes a few properties of these rotating models. We list the model names, the shear energy at bounce and 500 ms after bounce, and the ratio of total rotational energy to total gravitational energy ( $\beta^{\text{Rot}}$ ) initially, at bounce, and 500 ms after bounce. In §7, we describe results from these models when viscous dissipation is included.

Figure 2 shows the neutrino luminosity (left panels, in units of  $10^{52} \text{ erg s}^{-1}$ ) and average rms neutrino energy (right panels, in MeV) at infinity as a function of time relative to hydrodynamical bounce for each of our rotating models. Solid lines are for the  $11 M_\odot$  progenitor of Woosley & Weaver (1995). Dashed lines are for model E15A from Heger et al. (2000). Specifications for the models are given in §3 and Table 1. Note that in none of the models shown here is a centrifugal barrier reached during collapse. All models undergo bounce near the nuclear phase transition in the inner core and have sub-Keplerian rotational velocities throughout the computational domain. For clarity of presentation, the peak of the breakout pulse of electron neutrinos is not shown in the upper-left panel. The most rapid rotator ( $P_0 = 1.25 \text{ s}$ ) yields  $L_{\nu_e}^{\text{peak}} \simeq 3.1 \times 10^{53} \text{ erg s}^{-1}$ , whereas both E15A and the model with  $P_0 = 2 \text{ s}$  have  $L_{\nu_e}^{\text{peak}} \simeq 2.6 \times 10^{53} \text{ erg s}^{-1}$ . All other models have  $L_{\nu_e}^{\text{peak}} \simeq 2.4 \times 10^{53} \text{ erg s}^{-1}$ .

As expected, we find that the higher the initial rotation rate, the lower the core temperatures of the PNS formed just after bounce. On average, after electron neutrino breakout, this effect produces lower core  $L_\nu$  and  $\langle \varepsilon_\nu \rangle$  for shorter  $P_0$ . This reflects the sensitivity of the neutrino emissivities to the local temperature. The fractional differences in  $\langle \varepsilon_\nu \rangle$  between the model with  $P_0 = 1.25 \text{ s}$  and a non-rotating model 200 ms after bounce are approximately 15%, 17%, and 30% for  $\nu_\mu, \bar{\nu}_e$ , and  $\nu_e$ , respectively. The same comparison for  $L_\nu$  yields fractional differences of 75%, 63%, and 33% for  $L_{\nu_\mu}, L_{\bar{\nu}_e}$ , and  $L_{\nu_e}$ , respectively. The difference in  $L_{\nu_\mu}$  at 100 ms after bounce between our slowest and fastest rotators is a factor of  $\sim 6$ . The neutrino spectral characteristics change significantly and systematically as a function of  $P_0$ . Despite the fact that model E15A has rapid rotation, it has a much larger  $L_{\nu_e}$  after breakout than, for example, the  $P_0 = 2 \text{ s}$   $11 M_\odot$  model, even though they have similar initial  $\Omega(r)$  profiles (see Fig. 1). This is due to the extended density profile of model E15A relative to the  $11 M_\odot$  model and the associated larger accretion luminosity.

Figure 3 shows radial profiles of a number of quantities in a subset of the models of Fig. 2 at a time-slice 105 ms after bounce. The upper left panel shows the mass accretion rate for the models with  $P_0 = 1.25$  (dotted), 2 (dashed), 3 (dot-dashed), and 8 seconds (solid). The shock is clearly visible in each profile, the more rapid rotators having larger shock radii 105 ms after bounce. Higher negative  $\dot{M}$  implies larger PNS accretion rate and a larger accretion luminosity. This, coupled with the fact that the faster rotators achieve lower core temperatures at bounce, explains why the total luminosity is smaller for smaller  $P_0$  in Fig. 2. The upper right panel shows  $\Omega$  (positive numbers, in units of  $10^3 \text{ rad s}^{-1}$ ) and  $d\Omega/d\ln r$  (mostly negative numbers, in units of  $10^3 \text{ rad s}^{-1}$ ). The same line styles are employed. Note that the surface of the PNS (the neutrinosphere at the peak of the  $\nu_e$  spectrum) in this epoch lies at approximately 50–70 km (depending upon  $P_0$ ). Thus, if the mantle were ejected at this instant, assuming strict angular momentum conservation, all models with  $P_0 \lesssim 8 \text{ s}$  form 10 km neutron stars with  $P < 10 \text{ ms}$ . In fact, the model with  $P_0 = 8 \text{ s}$  would have a final spin period of  $\sim 7 \text{ ms}$ . The model with  $P_0 = 2 \text{ s}$  would have a final angular velocity over  $10^4 \text{ rad s}^{-1}$ .

The lower left panel of Fig. 3 shows the saturation magnetic field strength if the MRI operates everywhere, obtained simply by equating the magnetic energy density with the azimuthal kinetic energy density (as in eq. 16). Figure 3 shows that at radii near 100 km magnetic fields in the range  $B_\phi \sim 10^{14} - 10^{15} \text{ G}$

would be generic to relatively slowly rotating progenitors (here typified by the  $P_0 = 8$  s calculation, solid line). For rapid rotators, much of the core has field strengths of  $\sim 10^{16}$  G and above. The results presented here for  $B_{\text{Sat}_\phi}$  are in rough agreement with the models of Akiyama et al. (2003), but much higher than those presented in Fryer & Warren (2004). Comparing our Fig. 3 with their Fig. 13 we find that our field strengths are generally larger by 4–5 orders of magnitude.

Although we have not included viscous dissipation in any of the models presented in this section, in the lower right panel of Fig. 3 we plot the magnitude of the viscous dissipation rate, assuming that the MRI operates everywhere. We combine eqs. (3) and (15) to obtain

$$\dot{q}_{\text{MRI}} = \xi_{\text{MRI}} \left( \frac{d\Omega}{d \ln r} \right)^2 = \alpha H^2 \Omega \left( \frac{d\Omega}{d \ln r} \right)^2, \quad (19)$$

where we take  $\alpha = 0.1$ . The solid box shows a range of representative net neutrino energy deposition rates in the region exterior to the PNS ( $60 < r < 200$  km). Typical net neutrino heating rates in the gain region are  $\dot{q}_\nu \sim 100$  MeV nucleon $^{-1}$  s $^{-1} \sim 9.6 \times 10^{19}$  erg g $^{-1}$  s $^{-1}$ . The box brackets the range  $10^{18.5} \leq \dot{q}_{\text{MRI}} \leq 10^{20.5}$  erg g $^{-1}$  s $^{-1}$ . Of course, between the surface of the PNS and the shock the net heating rate varies considerably, going from negative to positive at the gain radius  $R_g$ . This panel is meant merely to underscore that a first comparison shows that the neutrino heating rate and the viscous heating rate are comparable for rapid rotators. If enough shear is present so that the energy deposition rate implied by the lower right panel of Fig. 3 can be maintained, the dynamics of the collapsed core may be significantly affected (§5.1). This is particularly true for more rapid rotation because the net neutrino heating rate in the gain region decreases as  $\Omega$  increases and the viscous heating rate increases as  $\Omega^3$ . Thus, the relative importance of viscous heating with respect to neutrino heating is compounded as the rotation rate increases.

For clarity of presentation we have not shown results for model E15A in Fig. 3. The saturation magnetic field strength and viscous dissipation rate for this model are very similar to the model with  $P_0 = 2$  s in the lower left and right panels, respectively. Model E15A has a larger negative  $\dot{M}$  at  $R_\nu$  and a larger  $R_\nu$  than model  $P_0 = 2$  s, but similar shock radius. Its shear and angular velocity profiles closely track those of model  $P_0 = 2$  s for  $r \gtrsim 20$  km. For  $r \lesssim 20$  km model E15A has  $\Omega > 10^4$  rad s $^{-1}$ , greater than the corresponding number for model  $P_0 = 1.25$  s. These differences between model E15A and model  $P_0 = 2$  s reflect the difference in initial  $\Omega(r)$  for  $r < 600$  km (Fig. 1) and the fact that the density profile for model E15A is much broader than that for  $P_0 = 2$  s.

### 5.1. Why Supernovae do not Explode in 1D

Figure 3 shows that the viscous heating via the MRI can be comparable to the net neutrino heating in the gain region. In §7, we will show that this effect is sufficient to yield explosions in some models. In order to address the question of why these models succeed, it is instructive first to consider why non-rotating spherical models with the very best physics fail. An elucidating and physical discussion of the stalled shock dynamics can be found in Janka (2001). We do not attempt to reproduce the detailed arguments presented there, but instead offer a semi-quantitative quasi-global criterion for explosion in the spirit of the arguments presented in Thompson (2000).

First, we define a radial advective timescale across a pressure scale height  $\tau_{\text{Adv}} = H/V_r$  and a timescale for net neutrino

heating  $\tau_{\dot{q}_\nu} = (P/\rho)/\dot{q}_\nu$ , where  $P$  is the thermal pressure,  $\rho$  is the mass density,  $\dot{q}_\nu = H_\nu - C_\nu$ , and  $H_\nu$  and  $C_\nu$  are the specific neutrino heating and cooling rates, respectively. Roughly speaking, steady-state accretion is maintained (explosions do not develop) in simulations of core-collapse in one dimension because  $\tau_{\text{Adv}} < \tau_{\dot{q}_\nu}$  in the gain region. If this were not the case (that is, if  $\tau_{\text{Adv}} > \tau_{\dot{q}_\nu}$ ), the thermal pressure would increase between  $R_g$  and  $R_{\text{sh}}$  (or, not decrease as quickly as material is advected into the cooling region) and the shock would move outward, finding a new equilibrium. This condition,  $\tau_{\text{Adv}} > \tau_{\dot{q}_\nu}$ , is a necessary but not sufficient condition to guarantee explosion. One must maintain the condition  $\tau_{\text{Adv}} > \tau_{\dot{q}_\nu}$  for a time sufficient to deposit roughly the binding energy of the overlying mantle,  $\sim 10^{51}$  erg. Thus, if the condition  $\tau_{\text{Adv}} > \tau_{\dot{q}_\nu}$  is met for  $t_i < t < t_f$  and

$$E_{\text{binding}}^{\text{mantle}} < \int_{t_i}^{t_f} \int \dot{q}_\nu \rho d^3 r dt, \quad (20)$$

then the mantle is unbound and an explosion results. The statement of eq. (20) is equivalent to saying that the matter achieves the "escape" temperature, obtained by equating the local specific thermal energy with the gravitational potential energy (Burrows & Goshy 1993; Burrows, Hayes, & Fryxell 1995).

We illustrate these basic numbers in Fig. 4, which shows  $\tau_{\dot{q}_\nu}$  (solid line),  $\tau_{\text{Adv}}$  (dashed line),  $\tau_{C_\nu} = (P/\rho)/C_\nu$  (dotted line), and  $\tau_{H_\nu} = (P/\rho)/H_\nu$  (dot-dashed line) for a slowly rotating initial progenitor ( $P_0 = 8$  s, see Fig. 2) 130 ms after bounce. The  $\nu_e$  neutrinosphere ( $R_{\nu_e}$ ) and the gain radius ( $R_g$ , where  $\tau_{C_\nu}$  crosses  $\tau_{H_\nu}$  and  $\tau_{\dot{q}_\nu}$  diverges) are indicated by arrows at this snapshot in time. Note that throughout the gain region ( $r > R_g$ )  $\tau_{\text{Adv}} < \tau_{\dot{q}_\nu}$ . The condition for explosion we suggest does not obtain. Following the evolution in this model for another 400 ms,  $\tau_{\dot{q}_\nu}/\tau_{\text{Adv}}$  is always greater than 1 at its minimum (which usually occurs very near, but exterior to,  $R_g$ ). We find very similar absolute values for the various timescales and ratios  $\tau_{\dot{q}_\nu}/\tau_{\text{Adv}}$  for all models that fail to explode. Of course, one may argue that the actual value of, for example,  $\tau_{\text{Adv}}$ , depends on its definition and that it may differ by order unity from that presented in Fig. 4. For example, we define  $\tau_{\text{Adv}}$  as  $H/V_r$  rather than  $r/V_r$  because  $\dot{q}_\nu$  depends fairly sensitively on radius near  $R_g$  since the cooling rates are highly dependent on the local temperature. Thus, the distance over which  $\dot{q}_\nu$  doubles near  $R_g$  is closer to  $H$  than  $r$ . This motivates our definition of  $\tau_{\text{Adv}}$ , but there is no reason *a priori* that  $\tau_{\text{Adv}}$  should not differ from  $H/V_r$  by, say, a factor of  $\sim 2$ . In addition,  $\tau_{\dot{q}_\nu}$  as we have defined it corresponds to an  $e$ -folding time for the local pressure, a relatively large change in the gain region. It may be that well before a full  $e$ -folding of  $P$  is accomplished the system adjusts. This is particularly true because the dynamical timescale ( $\tau_{\text{Dyn}} = H/c_s$  or  $r/c_s$ ) is much shorter than all other timescales. Thus, we cannot rule out order unity corrections to  $\tau_{\dot{q}_\nu}$ . For these reasons, that the ratio  $\tau_{\dot{q}_\nu}/\tau_{\text{Adv}}$  is  $\sim 1.3$  at  $r \sim 125$  km does not necessarily imply that if the net heating rate is increased by  $\sim 30\%$  the shock must begin to move outward. However, the ratio  $\tau_{\dot{q}_\nu}/\tau_{\text{Adv}}$  is certainly indicative of the magnitude of the deficit in heating that must be paid for explosion. Remarkably, we show in §7 that the criterion advocated here is quantitatively useful for assessing when explosions will develop.

Although simplistic, the picture presented here, which corresponds in rough terms with the conditions derived in Janka (2001), yields predictive power. In *all* of our spherical, non-rotating models (see Thompson et al. 2003)  $\tau_{\text{Adv}}$  is always less

than  $\tau_{\dot{q}_\nu}$  in the gain region over the full post-bounce evolution. Similarly, in model E15A and the models with  $P_0 = 2, 3, 4, 5$ , and 8 seconds, despite the wide range of mass accretion rates and post-bounce structures, the shock stalls in each model for the duration of the calculation and  $\tau_{\text{Adv}}/\tau_{\dot{q}_\nu}$  is always less than unity (when dissipation is not included).<sup>9</sup> Exceptions to this rule occur only during very dynamic episodes. For example, the instant the Si shell encounters the shock, the density decreases,  $\dot{M}$  decreases, and the shock moves out. In the instant between the two epochs of quasi-steady-state accretion,  $\tau_{\text{Adv}}$  can be greater than  $\tau_{\dot{q}_\nu}$ , but this is a transient and although the shock moves outward in radius, no explosion is obtained. In marked contrast, if one injects energy into the gain region, say via viscous dissipation with rate  $\dot{q}_{\text{MRI}}$ , then the relevant comparison is between  $\tau_{\text{Adv}}$  and  $\tau_{\dot{q}_{\text{TOT}}} = (P/\rho)/\dot{q}_{\text{TOT}}$ , where  $\dot{q}_{\text{TOT}} = H_\nu - C_\nu + \dot{q}_{\text{MRI}}$ . Adding  $\dot{q}_{\text{MRI}}$  to  $\dot{q}_\nu$  decreases the net heating timescale from  $\tau_{\dot{q}_\nu}$  to  $\tau_{\dot{q}_{\text{TOT}}}$ . If  $\dot{q}_{\text{MRI}}$  is large enough to yield  $\tau_{\dot{q}_{\text{TOT}}} < \tau_{\text{Adv}}$  and condition eq. (20) is met, an explosion results. We show in §7 that this mechanism succeeds.

## 6. COMPARING VISCOSUS PROCESSES

In this section we compare quantitatively the magnitude of the neutrino viscosity with the turbulent viscosity of the MRI in the dense protoneutron star core where neutrinos are diffusive. We also compare the linear growth rate for purely hydrodynamical convection and the MRI in the semi-transparent gain region with the neutrino damping rate. There have been a number of papers concerning the possibility that convection persists in PNS interiors during the accretion/explosion phase and afterwards, during Kelvin-Helmholtz cooling (Mayle 1985; Mayle & Wilson 1988; Wilson & Mayle 1988; Burrows 1987; Burrows & Lattimer 1988; Thompson & Duncan 1993; Keil & Janka 1995; Pons et al. 1999; Thompson & Murray 2001). If the neutrino viscosity ( $\xi_\nu$ ) is comparable to or larger than the viscosity of the MRI ( $\xi_{\text{MRI}}$ ) or convection, any turbulent fluctuations generated by these instabilities may be damped. Similarly, convective or magneto-convective modes in the gain region may also be damped if the neutrino damping rate ( $\Gamma_\nu$ ) is larger than the linear growth rates for convection ( $\sqrt{|N^2|}$ ) or the MRI ( $\Gamma_{\text{MRI}} \sim \Omega$ ).

In Fig. 5 we plot  $\xi_\nu$ ,  $\xi_{\text{MRI}}$ ,  $\Gamma_\nu$ ,  $\Gamma_{\text{MRI}}$ , and  $\sqrt{|N^2|}$  for the model with  $P_0 = 2$  s at a time 105 ms after bounce, as in Fig. 3. The left panel shows  $\xi_\nu$  for each neutrino species and  $\xi_{\text{MRI}}$  in the inner region of the PNS, inside the neutrinospheres for  $\nu_e$  and  $\bar{\nu}_e$  neutrinos at their respective spectral peaks. In this diffusive regime  $\langle \lambda_\nu \rangle$  is less than or much less than  $H$  and a comparison between the neutrino viscosity and the turbulent viscosity of the MRI is appropriate. For the purposes of comparison we have taken  $\xi_{\text{MRI}} = \alpha H^2 \Omega$  with  $\alpha = 0.1$ . The viscosity caused by the MRI clearly dominates neutrino viscosity by 2–3 orders of magnitude over the entire profile. Thus, within the PNS, when the condition for instability to the MRI is met (eq. 12), the MRI will operate and dominate the viscosity. Even for the slowest rotator considered here ( $P_0 = 8$  s),  $\xi_{\text{MRI}}$  is greater than  $\xi_\nu$  by an order of magnitude or more throughout the PNS interior.

In the right panel of Fig. 5 we plot  $\Gamma_\nu$  for each neutrino species and  $\Gamma_{\text{MRI}}$  as a function of radius in the semi-transparent region from roughly the surface of the PNS out to the shock

<sup>9</sup>The model with  $P_0 = 1.25$  s never develops a well-defined gain region and the shock never stalls completely. The centrifugal support (the decrease in the gravitational potential) as the shock is launched is sufficient to keep the shock moving, even though Keplerian rotational velocities are not obtained anywhere in the calculation. Matter velocities never exceed  $2 \times 10^8 \text{ cm s}^{-1}$  during the calculation and the internal energy of the ejected matter is small because there is little, if any, neutrino heating as the explosion develops. Roughly estimating the asymptotic energy, we obtain  $< 10^{50} \text{ erg}$ .

radius. Again, the linear growth rate of the MRI dominates the neutrino damping rates. At  $r \sim 50 \text{ km}$  the ratio  $\Gamma_{\text{MRI}}/\Gamma_\nu \simeq 10$ . In the gain region ( $r \sim 150 \text{ km}$ ), where the comparison is most important (that is where condition eq. 12 is always met)  $\Gamma_{\text{MRI}}/\Gamma_\nu \simeq 10^3$ . For the model with  $P_0 = 8$  s,  $\Gamma_{\text{MRI}}/\Gamma_\nu \sim 100$  in the gain region. For comparison, we also show the linear growth rate for convection ( $\sqrt{|N^2|}$ , dot-dashed line). As  $P_0$  decreases in our progenitor,  $\sqrt{|N^2|}$  in the gain region stays roughly constant while  $\Gamma_{\text{MRI}}$  decreases. In the model with  $P_0 = 8$  s,  $\sqrt{|N^2|}/\Gamma_{\text{MRI}} \sim 10$  at  $t \sim 100 \text{ ms}$  after bounce, at  $r \sim 150 \text{ km}$ . Importantly, both  $\Gamma_{\text{MRI}}$  and  $\sqrt{|N^2|}$  dominate  $\Gamma_\nu$  and we therefore expect well-developed, high Reynolds number convection/magneto-convection throughout the gain region in multi-dimensional models.

Although the profiles evolve considerably in time, in general, we find that much of the PNS core and all of the gain region is unstable to the MRI. In the cooling region just above the PNS ( $50 \text{ km} \lesssim r \lesssim 100 \text{ km}$ ),  $N^2$  in eq. (12) is sufficiently large and positive to counter much of the negative shear profile and the MRI is stabilized. However, we expect that a multi-dimensional simulation of the MRI in this context may show magneto-convective plumes and filaments penetrating the cooling region, as in the purely hydrodynamical calculations of Burrows, Hayes, & Fryxell (1995). Deeper in the PNS, beneath the  $\bar{\nu}_e$  neutrinosphere, the profile is unstable. The region  $20 \text{ km} \lesssim r \lesssim 50 \text{ km}$  is unstable to the MRI throughout most of the post-bounce epoch in the  $P_0 = 2$  s model. For slower initial rotation, this region of instability shrinks in radial extent. Imposing  $\Omega(r)$  as in eq. (4), we find that the very deep interior ( $r \lesssim 10 \text{ km}$ ) has positive or near-zero shear (see upper right panel of Fig. 3) and is stable to the MRI.

The region of very strong negative shear between  $10 \lesssim r \lesssim 20 \text{ km}$  in the upper right panel of Fig. 3 contains strong stabilizing entropy gradients and is stable over most of the evolution in all of the  $P_0$  models considered. Importantly, even though eq. (12) indicates that this region is stable to the MRI and convection, it is still possible to transport angular momentum and dissipate shear energy, albeit on a modified timescale (Spruit 2002). In stably stratified regions with differential rotation and a thermal diffusivity,  $\kappa$ , Spruit (2002) argues that magnetic interchange instabilities lead to an effective viscosity of (see his eq. 32)

$$\xi_S \sim H^2 \Omega \left( \frac{\Omega}{N} \right)^{1/2} \left( \frac{\kappa}{r^2 N} \right)^{1/2}, \quad (21)$$

where we have assumed a correlation length of  $H$  instead of  $r$ . Estimating  $\xi_S$  with  $\kappa = c \langle \lambda_\nu \rangle / 3$  and comparing with the left panel of Fig. 5, we find that in the region  $10 \lesssim r \lesssim 20 \text{ km}$   $\xi_S$  is less than  $\xi_{\text{MRI}}$  by approximately one order of magnitude and greater than  $\xi_\nu$  by approximately two orders of magnitude. This implies a viscous timescale of  $\tau_{\xi_S} = r^2 / \xi_S \sim 1–5 \text{ seconds}$  during the post-bounce epoch considered here. Interestingly,  $\tau_{\xi_S}$  may be different (possibly longer) than the Kelvin-Helmholtz timescale for late-time cooling.

Although the comparison of Fig. 5 shows that the two parts of the generalized Solberg-Høiland criterion are of similar magnitude, it is difficult to estimate the relative importance of convection versus the MRI in the non-linear regime without recourse to multi-dimensional simulations. Taking our estimates of the

turbulent viscosity for each process (eqs. 15 and 17) we have

$$\frac{\xi_{\text{Con}}}{\xi_{\text{MRI}}} = \frac{1}{3\alpha} \left( \frac{V_{\text{Con}}}{H\Omega} \right). \quad (22)$$

Taking  $V_{\text{Con}} \sim 5 \times 10^8 \text{ cm s}^{-1}$  as representative of the results from multi-dimensional simulations and  $H\Omega \sim 10^9 \text{ cm s}^{-1}$  ( $P_0 \lesssim 3 \text{ s}$ ) we see that for  $\alpha = 0.1$ ,  $\xi_{\text{Con}}$  and  $\xi_{\text{MRI}}$  are of the same order of magnitude. We reiterate, however, that even the sign of the convective stress is uncertain (§4.3) so the comparison presented here is quite simplistic.

## 7. CORE COLLAPSE WITH ROTATION & VISCOUS DISSIPATION

We now provide results from a subset of the rotating models considered in §5, including viscous dissipation and angular momentum transport.

The model with  $P_0 = 2$  seconds (see §5 and Figs. 1, 2, 3, and 5) serves to illustrate the effects of viscous dissipation most clearly. Without including dissipation, at 290 ms after bounce there is a well-defined gain region with  $R_g \simeq 115 \text{ km}$  and a shock radius of  $\sim 275 \text{ km}$ . The model is not exploding. It has timescale profiles very much like those in Fig. 4 for the model with  $P_0 = 8 \text{ s}$  with  $\tau_{\text{Adv}} < \tau_{\dot{q}_\nu}$  in the gain region (see §5.1). In this late post-bounce epoch we restart the calculation including viscous dissipation,  $\dot{q}_{\text{MRI}}$  with  $\alpha = 0.1$  (see eq. 19). The reason for restarting the simulation with dissipation nearly 300 ms after bounce instead of just 100 or 200 ms after bounce is that by this time in this progenitor the Si shell has fallen through the shock and the dynamical phase of shock expansion associated with this event is over. Because the system has settled into a steady-state accretion flow it is more easily diagnosed as we add heating by viscous dissipation. For this model, we include  $\dot{q}_{\text{MRI}}$  only in the region above the PNS surface for  $r \gtrsim 60 \text{ km}$ . Figure 6 shows the relative contributions to  $\dot{q}_{\text{TOT}} = \dot{q}_\nu + \dot{q}_{\text{MRI}}$  (solid line) at a time 300 ms after bounce. The heating rate from viscous dissipation ( $\dot{q}_{\text{MRI}}$ ), the total neutrino heating rate ( $\dot{q}_\nu$ ), and the contributions to  $\dot{q}_\nu$  from  $\nu_e$  and  $\bar{\nu}_e$  neutrinos are shown. In this model viscous heating extends into the neutrino cooling region, decreasing the net cooling just below  $R_g$ .

Complementary to Fig. 6, but more germane to the issue of explosion, is Fig. 7, in which we show all of the timescales presented in Fig. 4 and discussed in §5.1, but include  $\tau_{\dot{q}_{\text{MRI}}} = (P/\rho)/\dot{q}_{\text{MRI}}$  (short dashed line). We distinguish between  $\tau_{\dot{q}_\nu} = (P/\rho)/\dot{q}_\nu$  (dot-long dashed line) and  $\tau_{\dot{q}_{\text{TOT}}} = (P/\rho)/(\dot{q}_\nu + \dot{q}_{\text{MRI}})$  (solid line), where the former contains contributions only from neutrino heating and the latter includes both neutrino heating and viscous dissipation of shear energy. As shown clearly in Fig. 7, viscous dissipation is sufficient to make  $\tau_{\dot{q}_{\text{TOT}}}$  less than  $\tau_{\text{Adv}}$ . As per the discussion in §5.1 this is suggestive of a condition for a thermally-driven explosion. In this simulation and others, we find that if the condition  $\tau_{\text{Adv}}/\tau_{\dot{q}_{\text{TOT}}} > 1$  is met just outside  $R_g$ , the pressure increase is communicated to the rest of the gain region on a dynamical timescale and the shock expands. That the number on the right-hand-side of this inequality is so close to unity is surprising considering the ambiguities in defining  $\tau_{\text{Adv}}$  and  $\tau_{\dot{q}_{\text{TOT}}}$ . Nevertheless, we find that it is accurate. The region in Fig. 7 where  $\tau_{\text{Adv}}/\tau_{\dot{q}_{\text{TOT}}} > 1$  grows in time. The gain region expands as the shock moves outward. When the thermal energy of the gas exceeds the gravitational binding energy (and the escape temperature obtains) an explosion develops (eq. 20).

<sup>10</sup> Due to numerical limitations, including shock resolution and Courant-limited time stepping, it is difficult to push our calculations much beyond 800 ms after bounce.

The explosion is not driven by viscous dissipation alone. It is triggered by the combined action of  $\dot{q}_{\text{MRI}}$  and  $\dot{q}_\nu$ . In fact, just  $\sim 55$  milliseconds after the condition  $\tau_{\text{Adv}}/\tau_{\dot{q}_{\text{TOT}}} > 1$  is met in Fig. 7,  $\tau_{\text{Adv}}$  has increased enough so that  $\tau_{\dot{q}_\nu} < \tau_{\text{Adv}}$ . That is, neutrino heating alone is then sufficient to drive the explosion. In these  $\sim 55$  milliseconds  $\dot{q}_{\text{MRI}}$  deposits only  $\sim 4.1 \times 10^{49} \text{ erg}$  in the gain region. The neutrinos account for four times that (Fig. 6). This illustrates explicitly that any heating source that contributes an additional  $\sim 25 - 50\%$  to the net neutrino heating rate should be sufficient in most models to instigate explosion (see §5.1 and Fig. 4). In the model described here it takes  $\sim 160$  ms after the condition  $\tau_{\text{Adv}}/\tau_{\dot{q}_{\text{TOT}}} > 1$  is met for matter in the gain region to attain positive velocity. In this time period,  $\sim 8.5 \times 10^{49} \text{ erg}$  of shear energy is dissipated, whereas  $\sim 2.8 \times 10^{50} \text{ erg}$  is deposited by neutrinos. At the end, because the explosion is initiated at late times (we did not add  $\dot{q}_{\text{MRI}}$  until  $\sim 290$  ms after bounce), the extrapolated asymptotic energy of this explosion is rather small. Although we are not able to follow this calculation beyond  $\sim 760$  ms after bounce, taking rough account of the kinetic, thermal, and gravitational potential energies we estimate an asymptotic kinetic energy of  $\sim 2 \times 10^{50} \text{ erg}$ . Including the energy gained by recombination to nuclei of the  $\sim 0.02 M_\odot$  with positive velocities at the end of the calculation adds  $\sim 3.4 \times 10^{50} \text{ erg}$ , or a total asymptotic energy of  $\sim 5.4 \times 10^{50} \text{ erg}$ . Continued energy injection by neutrino heating will increase this estimate.

The matter ejected in this explosion has high electron fraction,  $Y_e$  (the number density of electrons per baryon). Figure 8 shows the time evolution of  $Y_e$  as a function of enclosed mass ( $M$ ) as the explosion develops. The dotted lines show deleptonization via  $e^- p \rightarrow n \nu_e$  as nuclei fall through the shock. The solid lines show  $Y_e(M)$  between the time the matter in the gain region attains positive velocity ( $t \simeq 460$  ms) and the end of the calculation ( $t \simeq 760$  ms). All of the matter outside  $M \simeq 1.408 M_\odot$  in the last time-slice shown has positive radial velocity. Most of the mass ejected has  $Y_e \geq 0.5$ , which should favor the production of  $^{56}\text{Ni}$  without anomalous production of Y, Zr, or Rb (as would be expected for lower  $Y_e$ ; Woosley & Hoffman 1992) – consistent with the results of Liebendörfer et al. (2003).

Similar numerical experiments may be carried out with different initial rotation periods and  $\alpha$ s. For larger  $\alpha$  and given  $P_0$ , the viscous time is shorter, shear energy is dissipated more rapidly (though roughly the same total energy is dissipated), the condition that  $\tau_{\text{Adv}}/\tau_{\dot{q}_{\text{TOT}}} > 1$  is more easily obtained, and explosions take less time to develop. For smaller  $\alpha$ , the threshold set by the condition  $\tau_{\text{Adv}}/\tau_{\dot{q}_{\text{TOT}}} > 1$  may not be reached or it may happen on a timescale too long to explore in the models presented here.<sup>10</sup> For example, taking  $\alpha = 0.01$ ,  $\dot{q}_{\text{MRI}}/\dot{q}_\nu \sim 0.03$  in the gain region for the  $P_0 = 2 \text{ s}$  model just considered (see Fig. 6),  $\tau_{\text{Adv}}/\tau_{\dot{q}_{\text{TOT}}} < 1$  throughout the gain region, and no explosion is obtained.

For shorter  $P_0$  (faster rotation), more shear energy is available in the gain region and at a given  $\alpha$  an explosion develops more quickly. In fact, the viscous heating rate at a given radius scales with  $\Omega^3$  and, all else being equal, if  $P_0$  is decreased from 2 s to 4 s, the heating rate in the gain region decreases by nearly an order of magnitude. Thus, beyond a threshold  $P_0$  ( $\sim 3 \text{ s}$ ) the difference between  $\tau_{\text{Adv}}$  and  $\tau_{\dot{q}_\nu}$  cannot be compensated for by including  $\dot{q}_{\text{MRI}}$  unless  $\alpha$  is much greater than 0.1.

It is perhaps artificial to begin including viscous dissipation so long after bounce. The purpose of the previous experiment was merely to clearly isolate the physics associated with shear energy dissipation. In reality, the magnetic field grows from an arbitrarily small seed field exponentially on a timescale  $\sim \Omega^{-1}$ . We expect a saturation magnetic field to obtain and fully developed magneto-convection to develop just 10–100 ms after bounce in the region exterior to the PNS. For this reason, we have run a number of models including  $\dot{q}_{\text{MRI}}$  after bounce, following the full evolution.

To this end, we conduct two tests with the model E15A (see §3.2, Table 1, and Figs. 1 and 2). In one case, we include viscous dissipation at all radii. In the second calculation we turn on viscous dissipation only when the generalized Solberg-Høiland criterion indicates that the region is unstable (eq. 12). This latter case is probably more realistic within the context of the spherical models presented in this paper. Both models employ  $\alpha = 0.1$  and do not transport angular momentum until after bounce. In both cases, we obtain explosions that develop on the relatively short timescale of  $\sim 100$  ms after bounce.

The explosions in this model are qualitatively different from the explosion obtained by waiting until a well-defined gain region forms and then adding viscous dissipation (Figs. 6–8). In non-exploding models, the bounce shock stalls immediately after formation, but then moves slowly outward in radius as the cooling and gain regions are formed until the shock reaches  $R_{\text{sh}} \sim 200$  km (about  $\sim 100$ –200 ms after bounce). Its outward progress is halted primarily by neutrino losses in the forming cooling region. Usually, the shock radius recedes slowly after reaching its maximum radius and sits for many hundreds of milliseconds at  $r \sim 150$  km. Indeed, this evolutionary sequence is borne out in model E15A without viscous dissipation; no explosion occurs. Including viscous heating in E15A, the evolution is very different. Neutrino losses behind the shock (as  $R_{\text{sh}}$  moves from  $\sim 80$  km to  $\sim 200$  km) are partially compensated by viscous heating. This extra energy deposition allows the shock to continue its outward progress, putting matter higher in the PNS gravitational well, and explosions are obtained. Because the shear in this model is rather large, the region behind the shock is unstable to the MRI and viscous dissipation operates. Stabilizing entropy gradients are insufficient to make  $N^2 + d\Omega^2/d\ln r$  positive (eq. 12). Because both the calculation with dissipation everywhere and the calculation respecting eq. (12) have viscous heating that partially compensates neutrino cooling as the shock is moving outward, the same qualitative evolution is obtained in both models. One important difference between them is that, on average, the model with dissipation throughout the profile has more heating behind the shock than the model that employs the generalized Solberg-Høiland criterion. This means that the explosion develops faster and leaves behind a less massive neutron star. Although we are able to follow only the first  $\sim 200$  ms after explosion ( $\sim 500$  ms after bounce), the difference between the PNS mass at the end of our simulations is roughly  $\sim 0.15 M_{\odot}$ , the larger baryonic mass being  $\sim 1.45 M_{\odot}$ .

Figure 9 shows the angular momentum evolution for the E15A model with dissipation at all radii as a function of the enclosed mass. For reference, the dotted line shows  $j_{\text{Kep}} = r^2 \Omega_{\text{Kep}}$  at bounce ( $t = 0$ ). The profile  $j(M)$  is shown at bounce and 22, 100, 200, and 350 ms after bounce. The transport of angular momentum is clear. For high viscosity,  $\Omega$  can decrease appreciably throughout the PNS core during explosion, pro-

viding a mechanism for at least partial spindown of the young PNS (Fryer & Warren 2004). Figure 9 can be compared with the three-dimensional simulations of Fryer & Warren (2004), who found significant angular momentum transport in the deep core of their rotating progenitors (see their Figs. 9 and 10). At  $M \sim 0.5 M_{\odot}$  they find that  $j$  decreases by a factor of  $\sim 4$  in  $\sim 200$  ms. We find a similar magnitude change in  $j$  at this  $M$ , implying that the magnitude of the intrinsic angular momentum transport in the simulations of Fryer & Warren (2004) is comparable to the transport caused here by our explicit viscosity, although the physical origin of the effective viscosity in their simulations is unclear.

Similar to the E15A models just described, we computed the evolution of the  $P_0 = 1.25, 2, 3$ , and  $4$  s models including viscous dissipation with  $\alpha = 0.1$ . Like the E15A models, we calculate a set of models with dissipation everywhere at all radii and a set of models respecting the generalized Solberg-Høiland stability criterion. All models with  $P_0 \leq 2$  s explode energetically. The model with  $P_0 = 3$  s and dissipation everywhere also explodes, but on a longer timescale. Both  $P_0 = 4$  s models and the model with  $P_0 = 3$  s and dissipation only in regions where the MRI is unstable do not. In these models, during the post-bounce epoch,  $\dot{q}_{\text{MRI}}$  was not large enough to force  $\tau_{\dot{q}_{\text{TOT}}} < \tau_{\text{Adv}}$  in the gain region. In addition, just after bounce the shear is not strong enough to drive the neutrino cooling region unstable to the MRI. For this reason, explosions qualitatively similar to the E15A models do not obtain.<sup>11</sup>

Typical results are shown in Figs. 10 and 11 for an exploding model with  $P_0 = 2$  s. The former shows snapshots of the velocity profile at various times during the development of explosion. The shock stalls and an accretion phase begins, but it never reaches a steady state. The constant injection of thermal energy by viscous dissipation keeps the pressure behind the shock relatively high and it moves out slowly, putting post-shock material higher in the PNS’s potential well. An explosion develops on a timescale of  $\sim 100$  ms after bounce. Figure 11 complements Fig. 10 by showing the full history of the mass element trajectories in time. The simulation is very well resolved; only every tenth mass zone is shown. Because the explosion is initiated early, and because the density profile for the  $11 M_{\odot}$  model is very steep, the mass of the PNS left behind is rather small  $\sim 1.27 M_{\odot}$  and the explosion energy is large. At the end of the calculation, the ejected matter has a kinetic energy of just  $2 \times 10^{50}$  erg, but an internal energy of  $\sim 2 \times 10^{51}$  erg. Models with larger  $P_0$  explode later and with less asymptotic energy.

As an aside, in Fig. 12 we provide two snapshots of the velocity profile (solid lines) in a representative exploding model. For comparison, we also include the sound speed profile. The two snapshots are separated by  $\sim 100$  ms in time and the shock moves from approximately 750 km to 2000 km. The large dot at  $\sim 850$  km marks the sonic point and the emergence of a transonic PNS wind (Duncan et al. 1986; Woosley et al. 1994; Takahashi, Witt, & Janka 1994; Burrows, Hayes, & Fryxell 1995). Profiles of entropy, mass loss rate, and electron fraction all show that a quasi-steady-state solution, quantitatively similar to that expected from the models of Thompson et al. (2001) and the analytic estimates of Qian & Woosley (1996) is obtained as the PNS begins the Kelvin-Helmholtz cooling epoch. In all of our successful exploding models, a transonic wind is formed. At the end of this calculation ( $P_0 = 2$  s,  $\alpha = 0.1$ ), 100 ms after the second snapshot in Fig. 12, the mechanical power

<sup>11</sup> Because we see qualitative differences between our models including viscosity with  $P_0 = 2$  s and  $P_0 = 3$  s (recall that  $\dot{q}_{\text{MRI}} \propto \Omega^3$ ; see lower-right panel of Fig. 3, eq. 19), we also ran a set of simulations with  $P_0 = 2.5$  s and  $\alpha = 0.1$ . These models also exploded, although on timescales somewhat longer than the  $P_0 = 2$  s models.

of the wind is  $\gtrsim 10^{50}$  erg s $^{-1}$ . If strong transonic PNS winds are a generic feature of the core-collapse supernova phenomenon, as implied by our calculations, this conclusion may have implications for late-time fallback and the mass cut (Woosley & Weaver 1995).

## 8. SUMMARY, CONCLUSIONS, & IMPLICATIONS

In this paper we forward the idea that some of the gravitational binding energy of core collapse may be trapped in differential rotation and that this free energy can be tapped on a viscous timescale ( $\sim 1$  s in the gain region) and deposited as thermal energy in the gas. We identify magnetic stresses generated by the magnetorotational instability as the most likely origin of this viscous energy dissipation. We have constructed models of core collapse, adding rotation and viscosity to our existing algorithm for spectral, multi-angle radiation hydrodynamics. We find that viscous dissipation can enhance the heating in the gain region sufficiently to yield explosions in models that would otherwise fail. Initial spin periods of the roughly solid-body iron core should be  $P_0 \lesssim 3$  seconds for this mechanism to be robust.

We emphasize several important points about this result. First, our simulations are one-dimensional and as such do not include the convective motions that have been shown to at least aid, if not enable, explosions (Herant et al. 1994; Burrows, Hayes, & Fryxell 1995; Janka & Müller 1996; Fryer et al. 1999; Janka et al. 2002; Buras et al. 2003). We expect that multi-dimensional models with *slower* initial progenitor rotation periods, including the effects of viscous dissipation consistently, will also yield explosions. Second, the effects of dissipation depend on where, when, and how quickly dissipation acts. Improved understanding of these issues will require MHD simulations and further progenitor modeling. Third, the values of  $P_0$  we require are fully consistent with the rotating progenitor models of Heger et al. (2000). However, there is considerable uncertainty in these rotation rates. In particular, the range  $P_0 \lesssim 3$  s is inconsistent with Heger et al. (2003), which attempted to include magnetic effects in calculating the angular momentum evolution of core-collapse progenitors. Finally, our limit on  $P_0$  is, at face value, inconsistent with the observed distribution of spin periods of young pulsars, which are in the range of many tens to many hundreds of milliseconds (Kaspi & Helfand 2002). Taking our successful explosion model with  $P_0 \sim 3$  s and extrapolating the spin period from our results to the fully-contracted neutron star radius of  $\sim 10$  km, we would be left with a neutron star with a  $\sim 2$  ms spin period. There is, of course, a danger in such comparisons since it is very difficult to pin down the true birth periods of neutron stars. It is also unclear if the spindown of very young neutron stars is well-understood theoretically as there are a number of ways to remove angular momentum from the neutron star during the explosion phase or the Kelvin-Helmholtz cooling epoch (§2). Given these uncertainties, we reiterate that the range of rotation rates considered here are expected theoretically in models of magnetar formation (Duncan & Thompson 1992; Thompson & Duncan 1993; Kouveliotou et al. 1999), a possibly large subset of all supernovae.

Our work has highlighted two primary impacts of rotation on the mechanism of core-collapse supernovae: 1) Most importantly, rotational kinetic energy tapped by viscous processes can help drive explosions (§7), and 2) Rotation lowers the effective gravity in the core, increasing the radius of the stalled shock and the size of the gain region (§5, Fig. 3). Since ejection is

inhibited by the deep potential well, this helps facilitate explosion. In addition to these, there are several multi-dimensional effects of rotation on core-collapse that remain to be fully explored (Burrows, Ott, & Meakin 2003): 1) Rotation might generate vortices that can dredge up heat from below the neutrinospheres and thereby enhance the driving neutrino luminosities. 2) Rotation can result in a large pole-to-equator anisotropy in the mass accretion rate after bounce due to the centrifugal barrier along the poles. Finally, 3) rotation results in pole-to-equator anisotropies in the driving neutrino flux that have never before been accurately calculated. Since the polar neutrino flux should be enhanced and the polar mass flux should be lowered (point 2), explosion along the poles with bipolar morphology seems that much more likely (Kotake, Yamada, & Sato 2003; Burrows & Goshy 1993; Burrows, Ott, & Meakin 2003). Thus, such bipolarity, and the consequent optical polarization of the debris, are not exclusive signatures of MHD-driven explosions (Akiyama et al. 2003; Symbalisty 1984), but may be a natural consequence of any rapidly rotating models.

In addition to the effects of rotation on the supernova mechanism, we have also shown how the observational signature of core collapse might be effected by rotation by identifying the systematics in the neutrino luminosity and average energy as a function of time, initial rotation rate, and progenitor (§5, Fig. 2). If the neutrino radiation from the next galactic supernova is observed in modern neutrino detectors like SuperKamiokande and SNO, we may hope to distinguish rapidly rotating core collapse via its neutrino signature. In addition to the difference highlighted in Fig. 2 we note that rapidly rotating models may leave an appreciable amount of shear energy ( $\sim 10^{52}$  erg) trapped in the inner core, which is stable to the MRI and convection. The timescale to dissipate this energy is uncertain, but could be  $\sim 1 - 10$  seconds or longer (eq. 21; Spruit 2002) as the PNS cools. The timescale for dissipation of this energy will likely differ from the Kelvin-Helmholtz timescale (Burrows & Lattimer 1986; Pons et al. 1999). Thus, rapidly rotating PNSs may have a unique long-timescale neutrino signature.

Finally, we have assessed the relative role of neutrino viscosity, the turbulent viscosity caused by the magnetorotational instability, and the viscosity of purely hydrodynamic convection. We find that, for the rotation rates considered here, the MRI and convection may be comparable in importance, but that both dominate microscopic neutrino viscosity everywhere and at all times during the collapse and accretion epochs. Turbulent magneto-convection should be generic for all modestly rotating progenitors and of critical importance to the dynamics of models with fairly rapid rotation,  $P_0 \lesssim 3$  s (Duncan & Thompson 1992; Thompson & Duncan 1993). Thus, in models with these rotation rates, magnetohydrodynamic effects should not be ignored. The simplicity of the algorithm employed here, which assumes spherical symmetry in a system that so clearly violates it and an  $\alpha$  viscosity, makes it clear that more work must be done to ascertain the full effects of MHD in rotating core collapse.

We gratefully acknowledge helpful conversations with Jon Arons, Anatoly Spitkovsky, and Yoram Lithwick. We thank Frank Timmes for making the Helmholtz EOS available. We also thank Alex Heger for providing rotating pre-collapse progenitors. T.A.T. is supported by NASA through Hubble Fellowship grant #HST-HF-01157.01-A awarded by the Space Telescope Science Institute, which is operated by the Association

of Universities for Research in Astronomy, Inc., for NASA, under contract NAS 5-26555. E.Q. is supported in part by NSF grant AST 0206006, NASA grant NAG5-12043, an Alfred P. Sloan Fellowship, the David and Lucile Packard Foundation,

and a Hellman Faculty Fund Award. A.B. is supported by the Scientific Discovery through Advanced Computing (SciDAC) program of the DOE, grant number DE-FC02-01ER41184.

## REFERENCES

Agol, E. & Krolik, J. 1998, *ApJ*, 507, 304  
 Akiyama, S., Wheeler, J. C., Meier, D. L., & Lichtenstadt, I. 2003, *ApJ*, 584, 954  
 Arras, P., Flanagan, E. E., Morsink, S. M., Schenk, A. K., Teukolsky, S. A., & Wasserman, I. 2003, *ApJ*, 591, 1129  
 Balbus, S. A. & Hawley, J. F. 1991, *ApJ*, 376, 214  
 Balbus, S. A. & Hawley, J. F. 1992a, *ApJ*, 392, 662  
 Balbus, S. A. & Hawley, J. F. 1992b, *ApJ*, 400, 610  
 Balbus, S. A. & Hawley, J. F. 1994, *MNRAS*, 266, 769  
 Balbus, S. A. & Hawley, J. F. 1998, *Rev. Mod. Phys.*, 70, No. 1  
 Bethe, H. & Wilson, J. 1985, *ApJ*, 295, 14  
 Bruenn, S. W. 1985, *ApJS*, 58, 771  
 Buras, R., Rampp, M., Janka, H.-Th., Kifonidis, K. 2003, *PRL*, 90, 241101  
 Burrows, A. & Lattimer, J. M. 1986, *ApJ*, 307, 178  
 Burrows, A. 1987, *ApJL*, 318, L57  
 Burrows, A. & Lattimer, J. M. 1988, *Physics Reports*, 163, 51  
 Burrows, A. & Gosh, J. 1993, *ApJL*, 416, L75  
 Burrows, A., Hayes, J., & Fryxell, B. A. 1995, *ApJ*, 450, 830  
 Burrows, A., Young, T., Pinto, P., Eastman, R., & Thompson, T. A. 2000, *ApJ*, 539, 865  
 Burrows, A. & Thompson, T. A. 2002, *Core-Collapse Supernovae*, Edited by C. L. Fryer, Kluwer Academic Publishers  
 Burrows, A., Ott, C.D., & Meakin, C. 2003, to be published in the proceedings of "3-D Signatures in Stellar Explosions: A Workshop honoring J. Craig Wheeler's 60th birthday," held June 10-13, 2003, Austin, Texas, USA  
 Chan, K. L. 2001, *ApJ*, 548, 1102  
 Duncan, R. C., Shapiro, S. L., & Wasserman, I. 1986, *ApJ*, 309, 141  
 Duncan, R. C. & Thompson, C. 1992, *ApJL*, 392, 9  
 Eastman, R. & Pinto, P. 1993, *ApJ*, 412, 731  
 Fryer, C. L., Benz, W., Herant, M., & Colgate, S. 1999, *ApJ*, 516, 892  
 Fryer, C. L. & Heger, A. 2000, *ApJ*, 541, 1033  
 Fryer, C. L. & Warren, M. S. 2002, *ApJL*, 574, L65  
 Fryer, C. L. & Warren, M. S. 2004, *ApJ*, 601, 391  
 Gunn, J. E. & Ostriker, J. P. 1969, *Nature*, 221, 454  
 Hawley, J. F., Gammie, C. F., & Balbus, S. A. 1996, *ApJ*, 464, 690  
 Heger, A., Langer, N., Woosley, S. E. 2000, *ApJ*, 528, 368  
 Heger, A., Woosley, S. E., Langer, N., & Spruit, H. C. 2003, *Stellar Rotation*, Proceedings IAU Symposium, No. 215, Edited by André Maeder & Philippe Eenens  
 Herant, M., Benz, W., Hix, W. R., Fryer, C. L., Colgate, S. A. 1994, *ApJ*, 435, 339  
 Horowitz, C. J. 1997, *Phys. Rev. D*, 55, 4577  
 Horowitz, C. J. 2002, *Phys Rev. D*, 65, 043001  
 Janka, H.-Th. & Müller, E. 1995, *ApJL*, 448, 109  
 Janka, H.-Th. & Müller, E. 1996, *A&A*, 306, 167  
 Janka, H.-Th. 2001, *A&A*, 368, 527  
 Janka, H.-Th., Buras, R., Kifonidis, K., Rampp, M., & Plewa, T. 2002, *Core Collapse of Massive Stars*, Ed. C. L. Fryer, Kluwer, Dordrecht, *Astro-ph/0212314*  
 Jedamzik, K., Katalinić, V., & Olinto, A. V. 1998, *PRD*, 57, 3264  
 Kaspi, V. M. & Helfand, D. J. 2002, *Neutron Stars in Supernova Remnants*, ASP Conference Series, Vol. 271, Edited by P. O. Slane & B. M. Gaensler  
 Käylä, P. J., Korpí, M. J., & Tuominen, I. 2003, submitted to *A&A*, *Astro-ph/0312376*  
 Keil, W. & Janka, H. Th. 1995, *A&A*, 296, 145  
 Khokhlov, A. M., Höflich, P. A., Oran, E. S., Wheeler, J. C., Wang, L., & Chtchelkanova, A. Y. 1999, *ApJL*, 524, L107  
 Kotake, K., Yamada, S., & Sato, K. 2003, *ApJ*, 595, 304  
 Kouveliotou, C., Strohmayer, T., Hurley, K., van Paradijs, J., Finger, M. H., Dieters, S., Woods, P., Thompson, C., Duncan, R. C. 1999, *ApJL*, 510, 115  
 Lattimer, J. M. & Mazurek, T. J. 1981, *ApJ*, 246, 955  
 Leblanc, J. M. & Wilson, J. R. 1970, *ApJ*, 161, 541  
 Liebendörfer, M., Mezzacappa, A., Thielemann, F.-K., Messer, O. E. B., Hix, W. R., & Bruenn, S. W. 2001a, *PRD*, 63, 103004  
 Liebendörfer, M., Mezzacappa, A., & Thielemann, F.-K. 2001b, *PRD*, 63, 104003  
 Liebendörfer, M., Messer, O. E. B., Mezzacappa, A., Bruenn, S. W., Cardall, C. Y., & Thielemann, F.-K. 2004, *ApJS*, 150, 263  
 Liebendörfer, M., Mezzacappa, A., Messer, O. E. B., Martinez-Pinedo, G., Hix, W. R., & Thielemann, F.-K. 2003, *Nuclear Physics A*, 719, 144  
 Lindblom, L., Tohline, J., & Vallisneri, M. 2001, *PRL*, 86, 1152  
 Livne, E., Burrows, A., Walder, R., Lichtenstadt, I., & Thompson, T. A. 2003, submitted to *ApJ*, *Astro-ph/0312633*  
 Mayle, R. 1985, Ph.D. Thesis, University of California, Berkeley  
 Mayle, R. & Wilson, J. R. 1988, *ApJ*, 334, 909  
 Mezzacappa, A. & Bruenn, S. W. 1993a, *ApJ*, 410, 637  
 Mezzacappa, A. & Bruenn, S. W. 1993b, *ApJ*, 410, 669  
 Mezzacappa, A. & Bruenn, S. W. 1993c, *ApJ*, 410, 740  
 Mezzacappa, A., Calder, A. C., Bruenn, S. W., Blondin, J. M., Guidry, M. W., Strayer, M. R., & Umar, A. S. 1998, *ApJ*, 493, 848  
 Mezzacappa, A., Liebendörfer, M., Messer, O. E. B., Hix, W. R., Thielemann, F.-K., & Bruenn, S. W. 2001, *PRL*, 86, 1935  
 Narayan, R., Quataert, E., Igumenshchev, I. V., Abramowicz, M. 2002, *ApJ*, 577, 295  
 Ostriker, J. P. & Gunn, J. E. 1969, *ApJ*, 157, 1395  
 Ott, C. D., Burrows, A., Livne, E., & Walder, R. 2003, *ApJ*, 600, 834  
 Pacini, F. 1967, *Nature*, 216, 567  
 Pacini, F. 1968, *Nature*, 219, 145  
 Pons, J. A., Reddy, S., Prakash, M., Lattimer, J. M., & Miralles, J. A. 1999, *ApJ*, 513, 780  
 Qian, Y.-Z. & Woosley, S. E. 1996, *ApJ*, 471, 331  
 Rampp, M. & Janka, H.-Th. 2000, *ApJL*, 539, 33  
 Rampp, M. & Janka, H.-Th. 2002, *A&A*, 396, 361  
 Shakura, N. I. & Sunyaev, R. A. 1973, *A&A*, 24, 337  
 Spruit, H. C. 2002, *A&A*, 381, 923  
 Spruit, H. C. & Phinney, E. S. 1998, *Nature*, 393, 139  
 Spruit, H. C. 2003, *Stellar Rotation*, Proceedings IAU Symposium, No. 215, Edited by André Maeder & Philippe Eenens  
 Stone, J. M., Hawley, J. F., Gammie, C. F., & Balbus, S. A. 1996, *ApJ*, 463, 656  
 Symbalisty, E. M. D. 1984, *ApJ*, 285, 729  
 Takahashi, K., Witti, J., & Janka, H.-T. 1994, *A&A*, 286, 857  
 Tassoul, J. L. 1978, in *Theory of Rotating Stars*, ed. J. Ostriker (Princeton: Princeton Univ. Press)  
 Thompson, T. A., Burrows, A., & Horvath, J. E. 2000, *PRC*, 62, 035802  
 Thompson, T. A. 2002, Ph.D. Thesis, The University of Arizona  
 Thompson, T. A., Burrows, A., & Pinto, P. A. 2003, *ApJ*, 592, 434  
 Thompson, T. A. 2003, *ApJL*, 585, L33  
 Thompson, T. A., Chang, P., & Quataert, E. 2004, *ApJ*, submitted, *Astro-ph/0401555*  
 Thompson, C. & Duncan, R. C. 1993, *ApJ*, 408, 194  
 Thompson, C. 2000, *ApJ*, 534, 915  
 Thompson, C. & Murray, N. 2001, *ApJ*, 560, 339  
 Timmes, F. X. & Swesty, F. D. 2000, *ApJS*, 126, 501  
 Timmes, F. X. & Arnett, D. 1999, *ApJS*, 125, 277  
 Van den Horn, L. J. & Van Weert, C. G. 1984, *Astron. Astrophys.*, 136, 74  
 Wilson, J. R. & Mayle, R. W. 1988, *Physics Reports*, 163, 63  
 Woosley, S. E., Wilson, J. R., Mathews G. J., Hoffman, R. D., & Meyer, B. S. 1994, *ApJ*, 433, 209  
 Woosley, S. E. & Hoffman, R. D. 1992, *ApJ*, 395, 202  
 Woosley, S. E. & Weaver, T. A. 1995, *ApJS*, 101, 181  
 Woosley, S. E. & Heger, A. 2003, *Stellar Rotation*, Proceedings of the IAU Symposium, No. 215, Edited by André Maeder & Philippe Eenens

TABLE I  
ROTATING CORE-COLLAPSE WITHOUT DISSIPATION

Name	$\beta_i^{\text{Rot}}$	$\beta_b^{\text{Rot}}$	$\beta_{500}^{\text{Rot}}$	$E_b^{\text{shear}} (10^{51} \text{ erg})$	$E_{500}^{\text{shear}} (10^{51} \text{ erg})$
$P_0 = 1.25 \text{ s}$	0.0035	0.059	0.070	21.8	32.9
$P_0 = 2.0 \text{ s}$	0.0014	0.028	0.039	11.4	25.0
$P_0 = 3.0 \text{ s}$	$6.0 \times 10^{-4}$	0.012	0.020	4.98	13.9
$P_0 = 4.0 \text{ s}$	$3.4 \times 10^{-4}$	0.0065	0.012	2.46	8.39
$P_0 = 5.0 \text{ s}$	$2.2 \times 10^{-4}$	0.0042	0.0077	1.61	5.56
$P_0 = 8.0 \text{ s}$	$8.5 \times 10^{-5}$	0.0017	0.0031	0.638	2.26
E15A	0.0020	0.053	0.067	20.6	49.7

$\beta^{\text{Rot}}$  is the ratio of the total rotational energy to the magnitude of the total gravitational energy. All " $P_0$ " models have  $R_\Omega = 1000 \text{ km}$  (see eq. 4). Subscripts  $i$ ,  $b$ , and 500 imply *initial*, *at bounce*, and *500 milliseconds after bounce*, respectively.

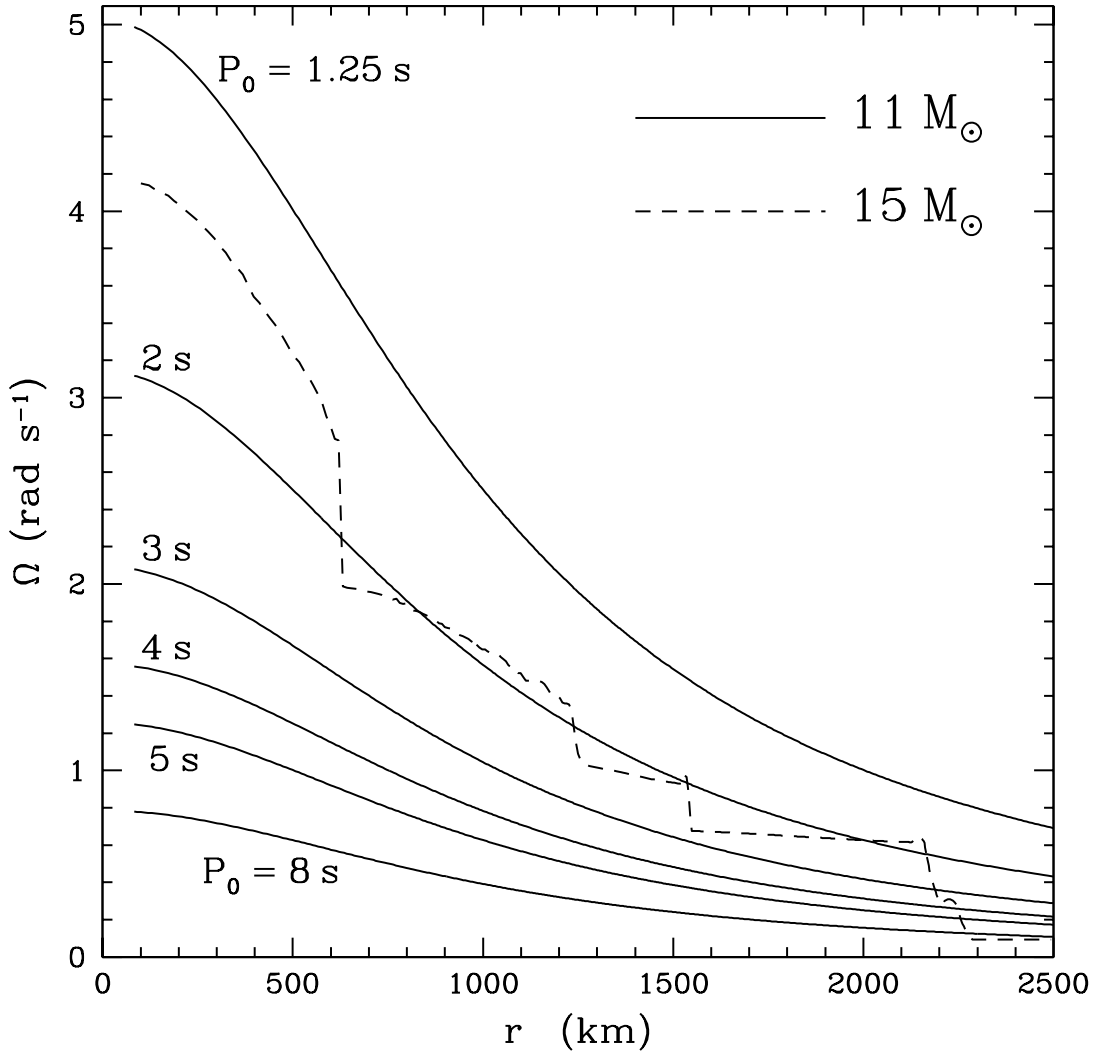


FIG. 1.— Initial angular velocity ( $\Omega$ ,  $\text{rad s}^{-1}$ ) as a function of radius for the models considered in this paper. The solid lines show the  $\Omega(r)$  profile imposed on the  $11 M_{\odot}$  model of Woosley & Weaver (1995) with  $R_{\Omega} = 1000$  km and  $P_0 = 1.25, 2, 3, 4, 5$ , and  $8$  seconds (see eq. 4). The dashed line shows the angular velocity profile for the model E15A from Heger et al. (2000). For simplicity, we refer to the Woosley & Weaver (1995) models by their initial " $P_0$ " and the Heger et al. (2000) model as "E15A".

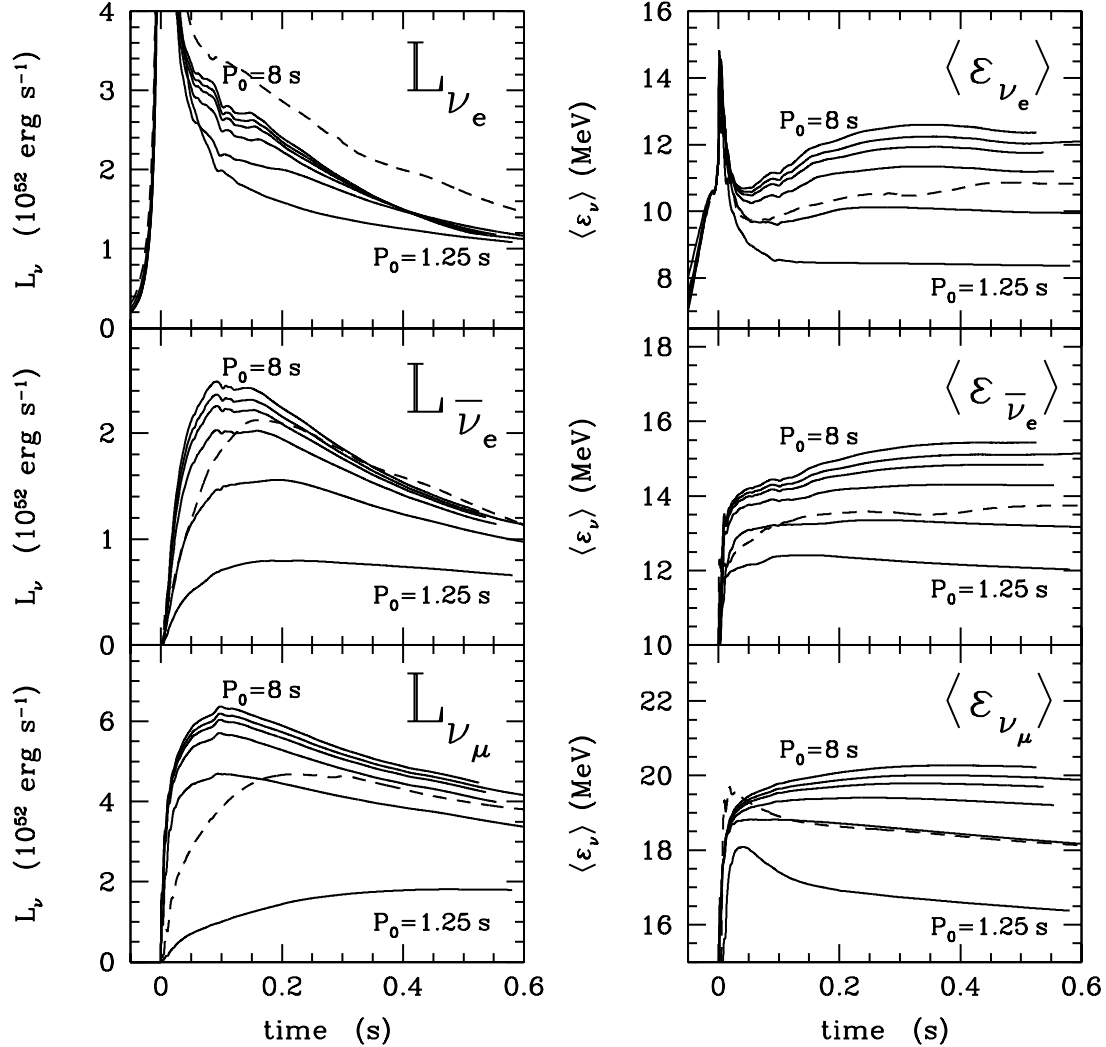


FIG. 2.— Neutrino luminosity ( $L_\nu$ , left panels) in  $10^{52} \text{ erg s}^{-1}$  and average neutrino energy ( $\langle \varepsilon_\nu \rangle$ , right panels) in MeV as a function of time after bounce for the rotating  $11 M_\odot$  models with  $P_0 = 1.25, 2, 3, 4, 5$ , and  $8 \text{ s}$  (solid lines). In all cases, at  $200 \text{ ms}$  after bounce, the lowest  $L_\nu$  and  $\langle \varepsilon_\nu \rangle$  correspond to the fastest initial rotation. Note that this hierarchy is preserved at all times and in all panels except in the case of  $L_{\nu_e}$   $400 \text{ ms}$  after bounce and at breakout. Although they cannot be directly compared with the  $11 M_\odot$  models, the results for the model E15A from Heger et al. (2000) are also shown (dashed lines, see Fig. 1) 1) The  $\nu_e$  breakout burst at  $t = 0$  (not shown here) is largest for the fastest rotator, with  $L_{\nu_e}^{\text{peak}} \simeq 3.1 \times 10^{53} \text{ erg s}^{-1}$ . For both E15A and the model with  $P_0 = 2 \text{ s}$ ,  $L_{\nu_e}^{\text{peak}} \simeq 2.6 \times 10^{53} \text{ erg s}^{-1}$ . For the slowest rotator we recover the non-rotating case and  $L_{\nu_e}^{\text{peak}} \simeq 2.4 \times 10^{53} \text{ erg s}^{-1}$ . See §5 for details.

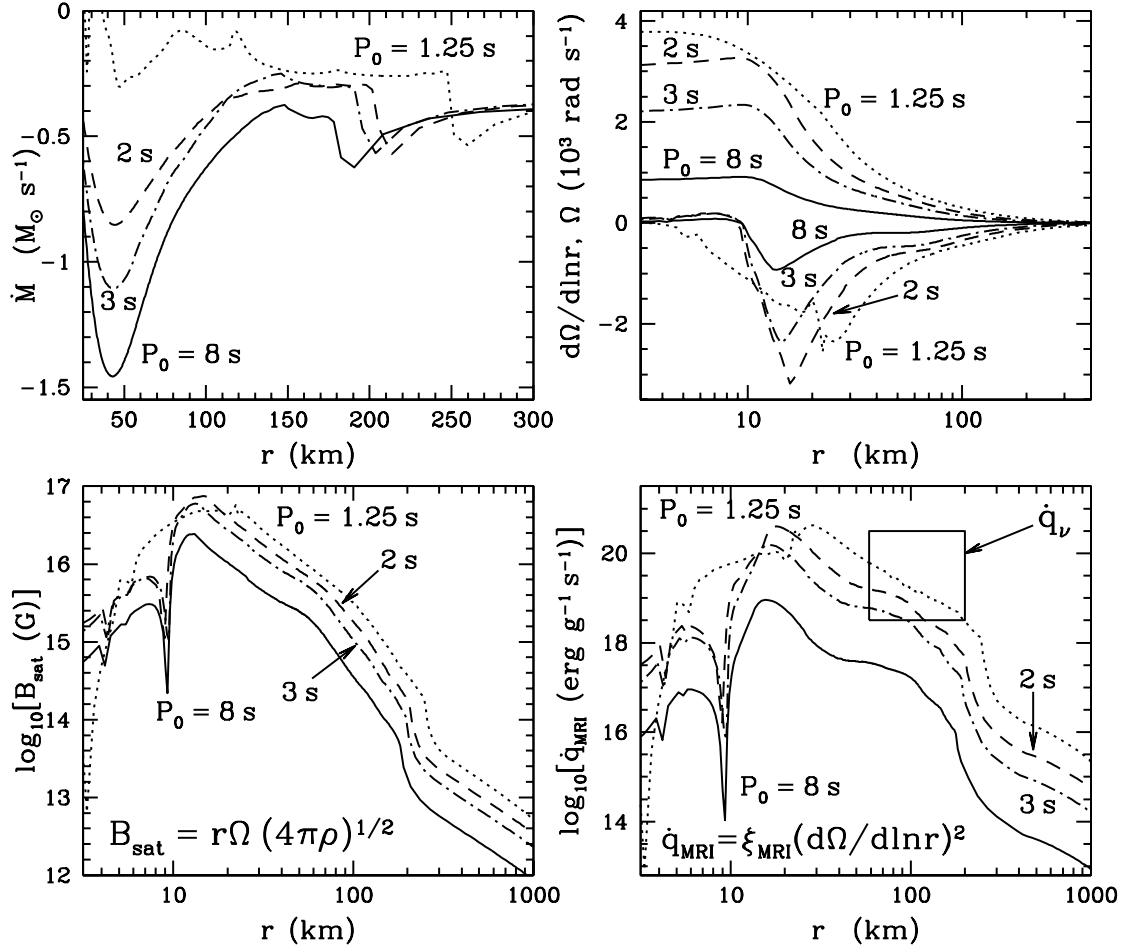


FIG. 3.— Mass accretion rate ( $\dot{M}$  [ $M_\odot \text{ s}^{-1}$ ], upper left panel), shear ( $d\Omega/d\ln r$ ) and  $\Omega$  ( $10^3 \text{ rad s}^{-1}$ , upper right panel), putative saturation magnetic field strength ( $\log_{10}[B_{\text{sat}} \text{ G}]$ , lower left panel), and viscous dissipation rate ( $\dot{q}_{\text{MRI}}$  [ $\text{erg g}^{-1} \text{ s}^{-1}$ ], lower right panel) versus radius in km for rotating models with  $P_0 = 1.25$  (dotted), 2 (dashed), 3 (dot-dashed), and 8 s (solid) at  $t = 105$  ms after bounce. These models did not include viscous dissipation. We show  $\dot{q}_{\text{MRI}}$  (with  $\alpha = 0.1$  in  $\xi_{\text{MRI}}$  as in eq. 15) only for comparison with typical neutrino heating rates in models of supernovae ( $\dot{q}_\nu$ , solid box). For clarity of presentation a different radial scale is used for each panel.

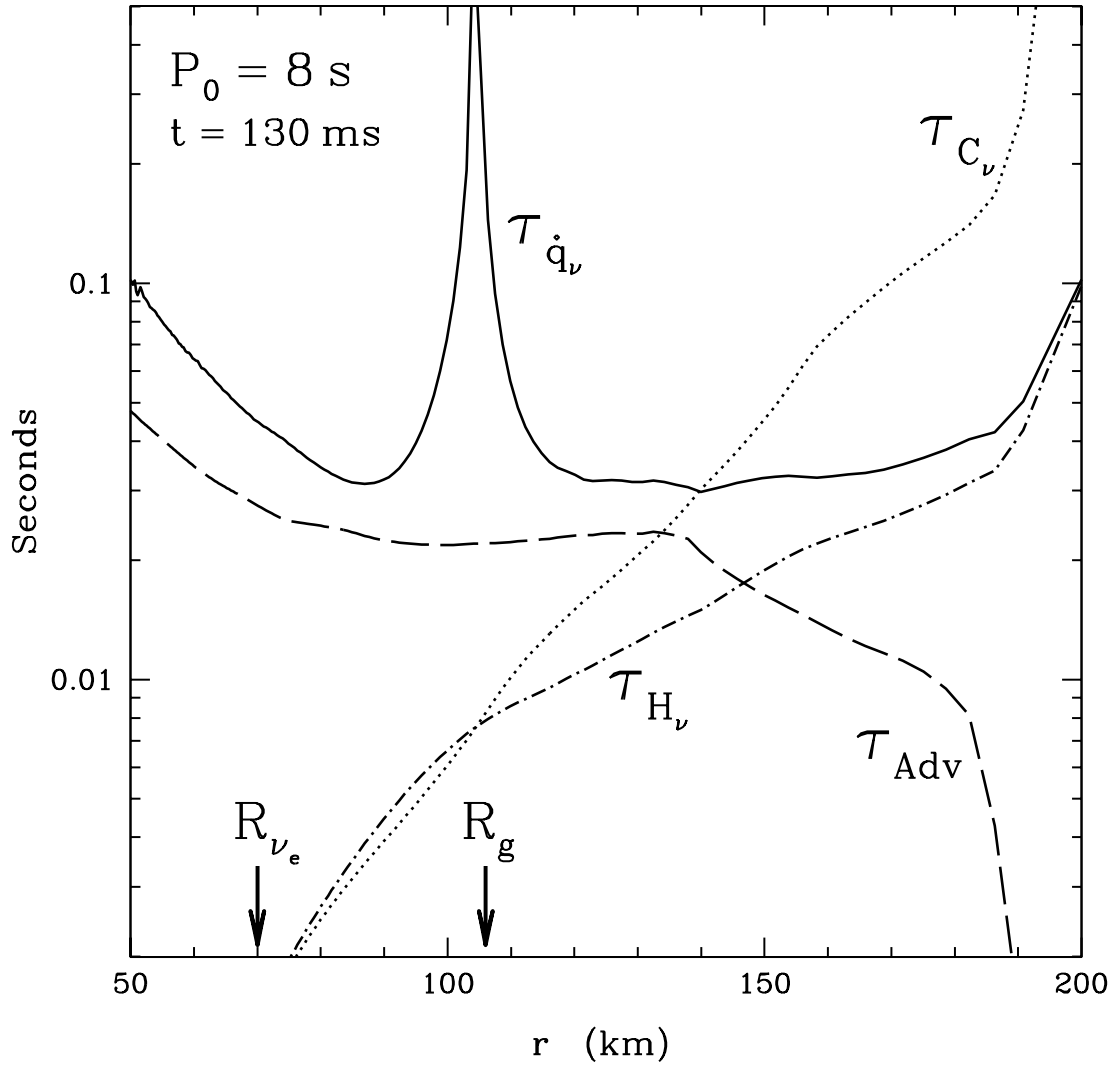


FIG. 4.— The neutrino heating timescale ( $\tau_{H_\nu} = (P/\rho)/H_\nu$ , dot-dashed line), neutrino cooling timescale ( $\tau_{C_\nu} = (P/\rho)/C_\nu$ , dotted line), net neutrino heating timescale ( $\tau_{\dot{q}_\nu} = (P/\rho)/\dot{q}_\nu$ , solid line), and the advection timescale ( $\tau_{\text{Adv}} = H/V_r$ , dashed line) in seconds, as a function of radius  $r$  (km) at a time 130 ms after bounce.  $R_{\nu_e}$  and  $R_g$  mark the  $\nu_e$  neutrinosphere (for  $\varepsilon_{\nu_e} \simeq 12$  MeV) and the gain radius, respectively.

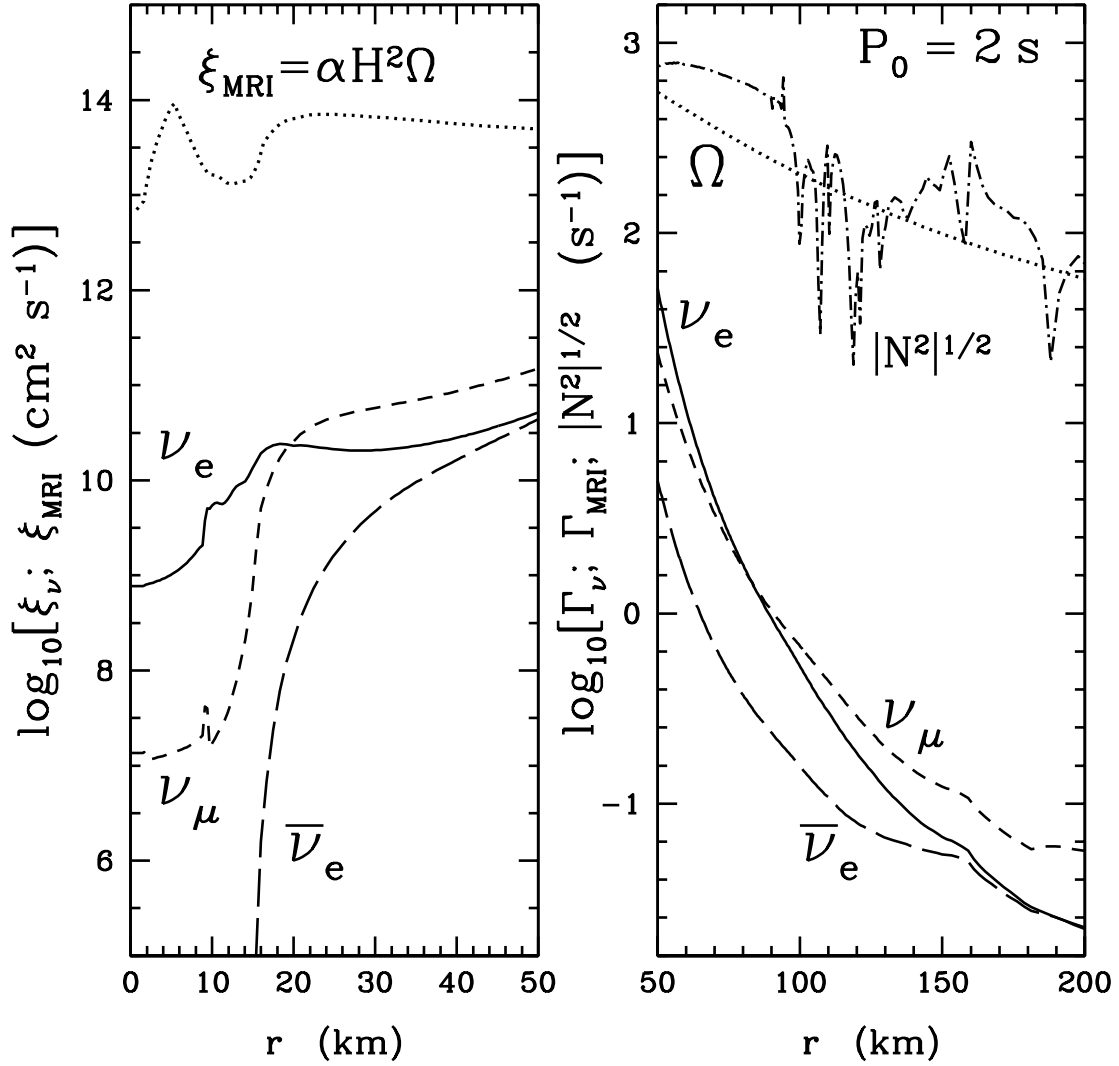


FIG. 5.— *Left Panel* - Microscopic shear viscosity of electron neutrinos (solid line), anti-electron neutrinos (long dashed line), and muon neutrinos (short dashed line) in the deep interior of a PNS  $\sim 105$  ms after bounce. For comparison, we show the effective viscosity due to the MRI (taking  $\alpha = 0.1$ ; dotted line), which dominates the total neutrino viscosity. *Right Panel* - Damping rate due to neutrino interactions ( $\Gamma_\nu$ ) and the optimal growth rate of the MRI ( $\Gamma_{\text{MRI}} \sim \Omega$ ) in the semi-transparent regime. The Brunt-Väisälä frequency  $\sqrt{|N^2|}$  is also shown.

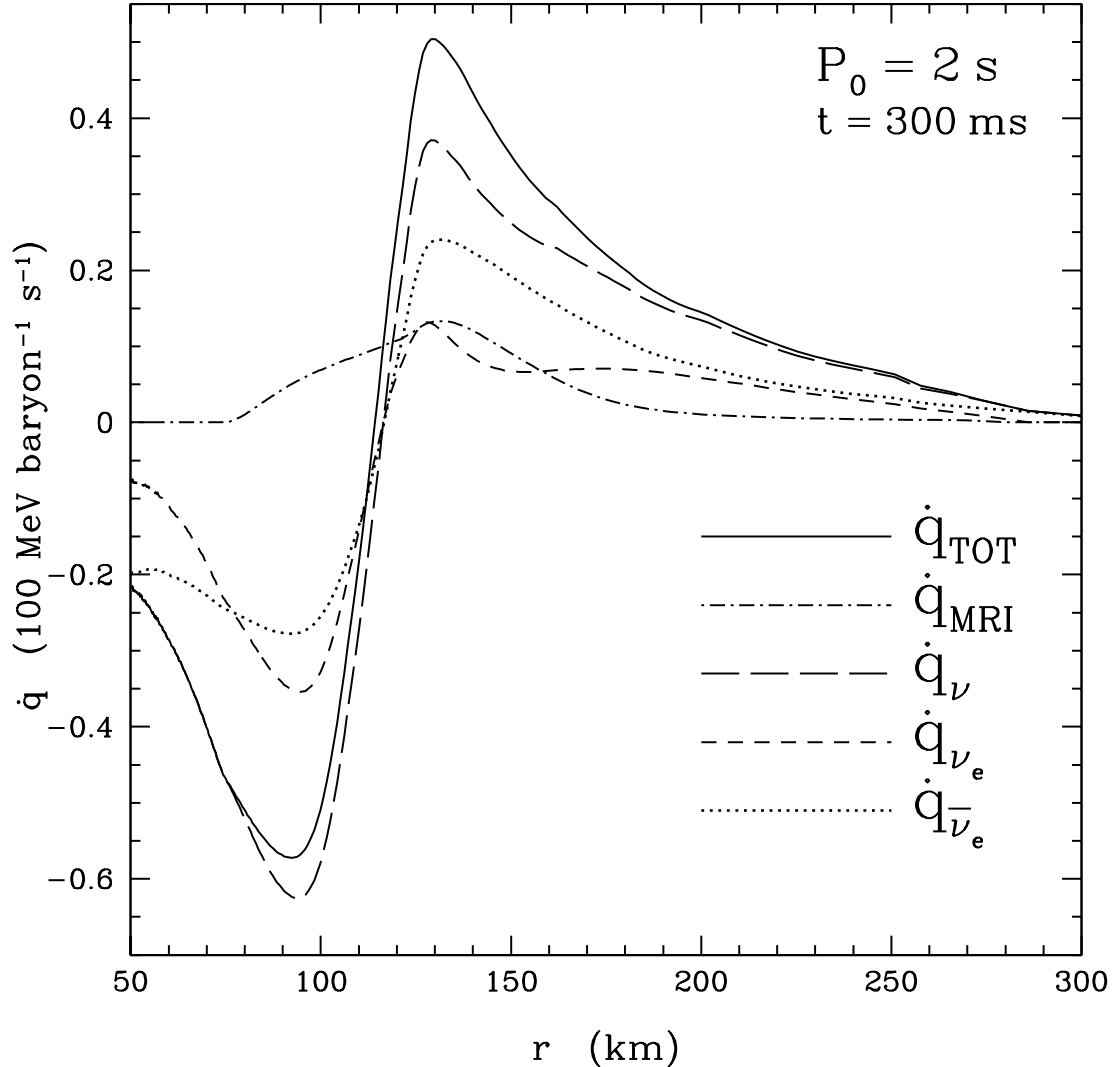


FIG. 6.— Energy deposition rate as a function of radius in units of  $100 \text{ MeV baryon}^{-1} \text{ s}^{-1}$  for the rotating model with  $P_0 = 2$  seconds, including viscous dissipation via the MRI with  $\alpha = 0.1$ . Total energy deposition rate ( $\dot{q}_{TOT} = \dot{q}_\nu + \dot{q}_{MRI}$ , solid line), viscous energy deposition rate ( $\dot{q}_{MRI}$ , eq. 19, dot-dashed line), and neutrino energy deposition rate ( $\dot{q}_\nu = H_\nu - C_\nu$ , long dashed line) are shown. For comparison, individual contributions to  $\dot{q}_\nu$  from  $\nu_e$  (short dashed line) and  $\bar{\nu}_e$  (dotted line) are also included.

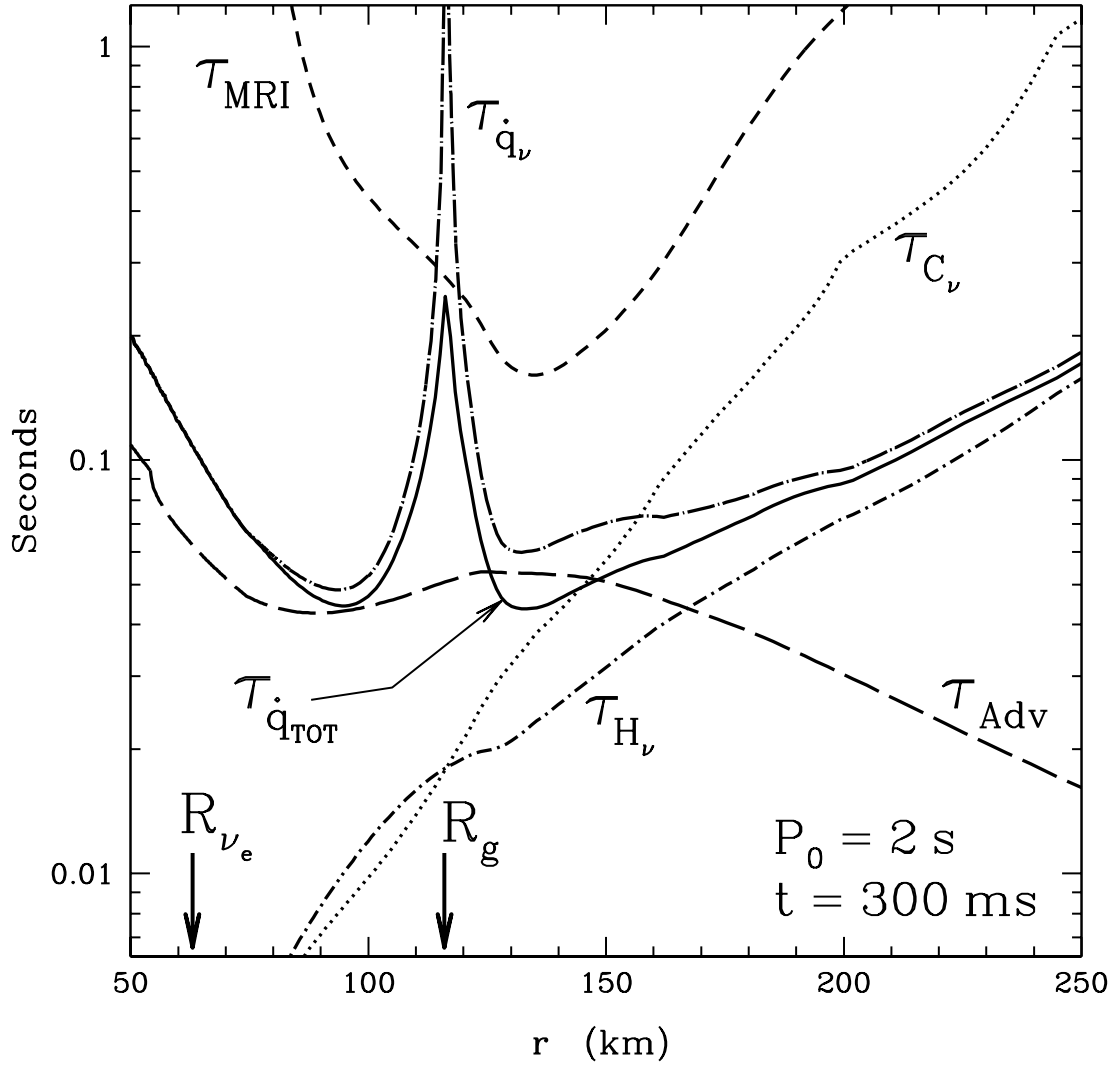


FIG. 7.— The neutrino heating timescale ( $\tau_{H_\nu} = (P/\rho)/H_\nu$ , dot-short dashed line), neutrino cooling timescale ( $\tau_{C_\nu} = (P/\rho)/C_\nu$ , dotted line), net neutrino heating timescale ( $\tau_{q_\nu} = (P/\rho)/\dot{q}_\nu$ , dot-long dashed line), the advection timescale ( $\tau_{\text{Adv}} = H/V_r$ , long dashed line), the viscous heating timescale for the MRI ( $\tau_{\text{MRI}} = (P/\rho)/\dot{q}_{\text{MRI}}$ , short dashed line), and the total heating timescale including viscous dissipation ( $\tau_{q_{\text{TOT}}} = (P/\rho)/(\dot{q}_\nu + \dot{q}_{\text{MRI}})$ , solid line) in seconds, as a function of radius  $r$  (km) at a time 300 ms after bounce in our  $11 M_\odot$  progenitor with  $P_0 = 2$  s.  $R_{\nu_e}$  and  $R_g$  mark the  $\nu_e$  neutrinosphere and gain radius, respectively. The shock radius is  $\sim 275$  km. Compare with Fig. 4. Note that exterior to  $R_g$ , as a result of  $\dot{q}_{\text{MRI}}$ ,  $\tau_{\text{Adv}}$  is greater than  $\tau_{q_{\text{TOT}}}$  (see §5.1 and §7).

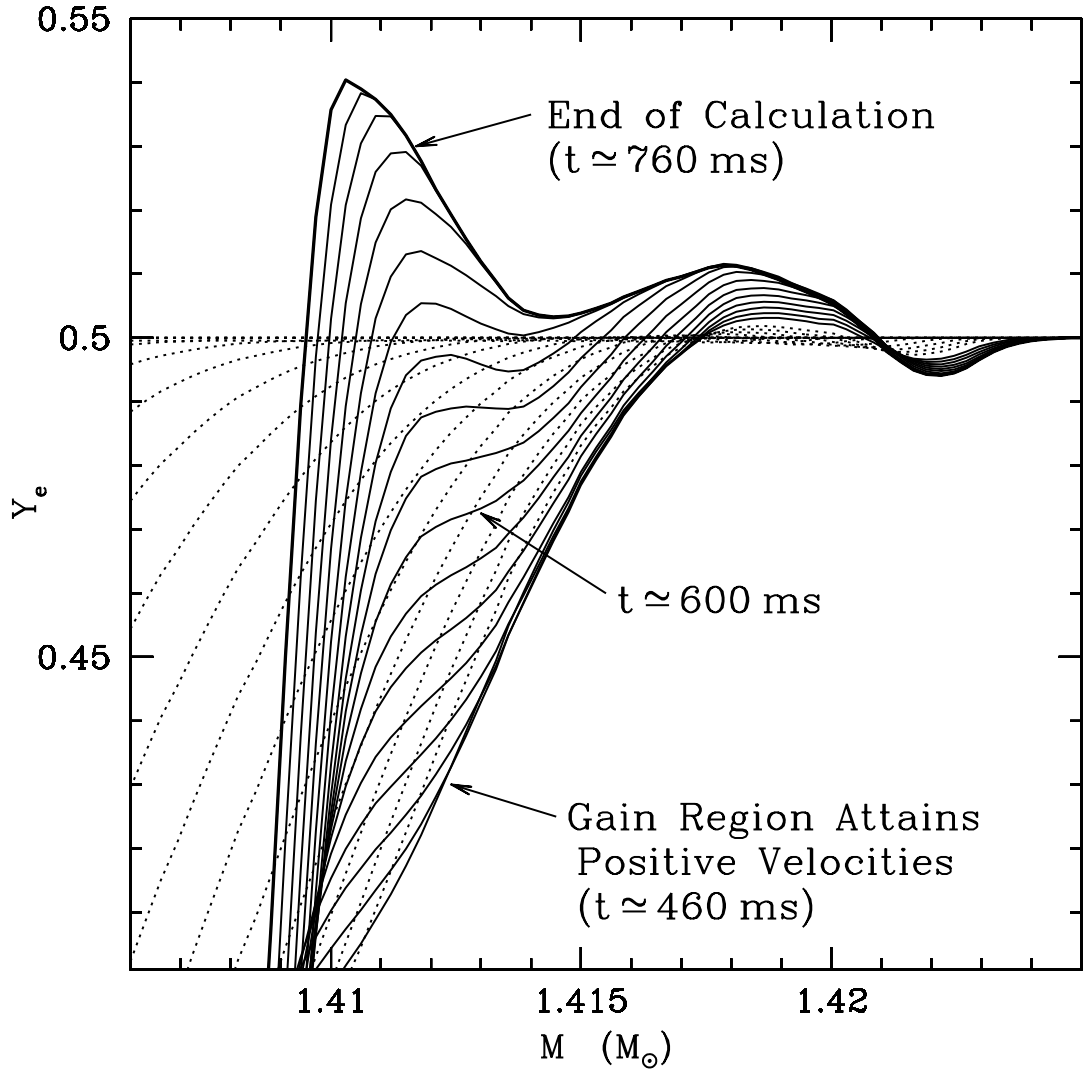


FIG. 8.— Electron fraction  $Y_e$  versus enclosed mass  $M$  ( $M_\odot$ ) at many snapshots in time in the exploding model with  $P_0 = 2$  s, restarted with viscous dissipation (see §7). The dotted lines show deleptonization as nuclei fall through the shock and dissociate. The solid lines show the evolution of  $Y_e(M)$  after positive velocities are attained in the gain region ( $t \simeq 460$  ms;  $\sim 160$  ms after the condition  $\tau_{\text{Adv}}/\tau_{q\text{TOT}} > 1$  is reached in the gain region; see Fig. 7) and until the end of the calculation ( $t \simeq 760$  ms). Times quoted are relative to bounce.

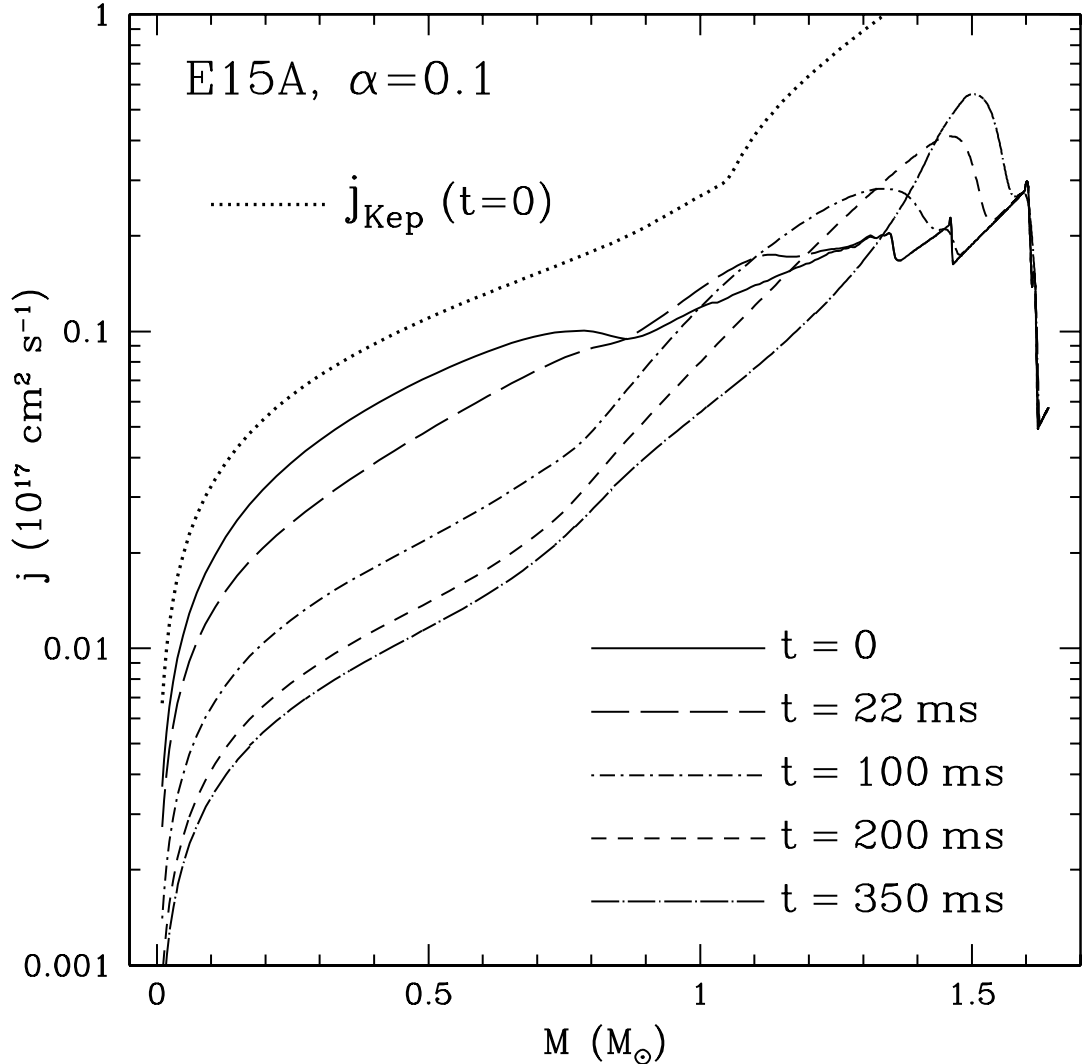


FIG. 9.—Angular momentum ( $j$ ,  $10^{17} \text{ cm}^2 \text{ s}^{-1}$ ) as a function of enclosed mass in the model E15A including viscous dissipation with  $\alpha = 0.1$  at bounce (solid line,  $t = 0$ ), 22 ms (long dashed line), 100 (dot-short dashed line), 200 (short dashed line), and 350 ms (dot-long dashed line) after bounce. For reference the Keplerian angular momentum profile  $j_{\text{Kep}} = r^2 \Omega_{\text{Kep}}$  at bounce ( $t = 0$ , dotted line) is also shown.

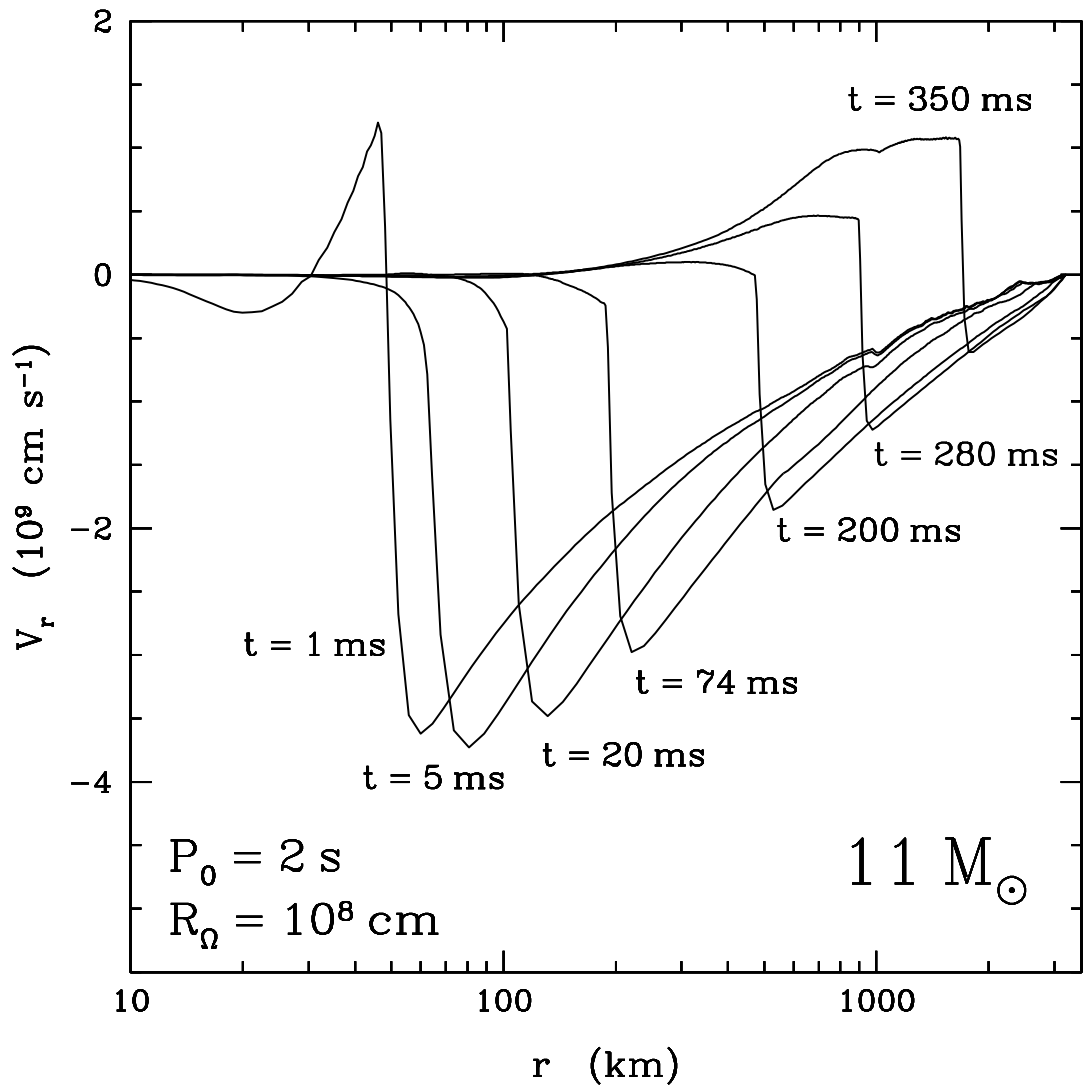


FIG. 10.— Radial velocity as a function of radius for various snapshots in time during the development of explosion in the  $11 M_\odot$  progenitor with  $P_0 = 2 \text{ s}$ , including viscous dissipation after bounce with  $\alpha = 0.1$  (see Figs. 11 and 12).

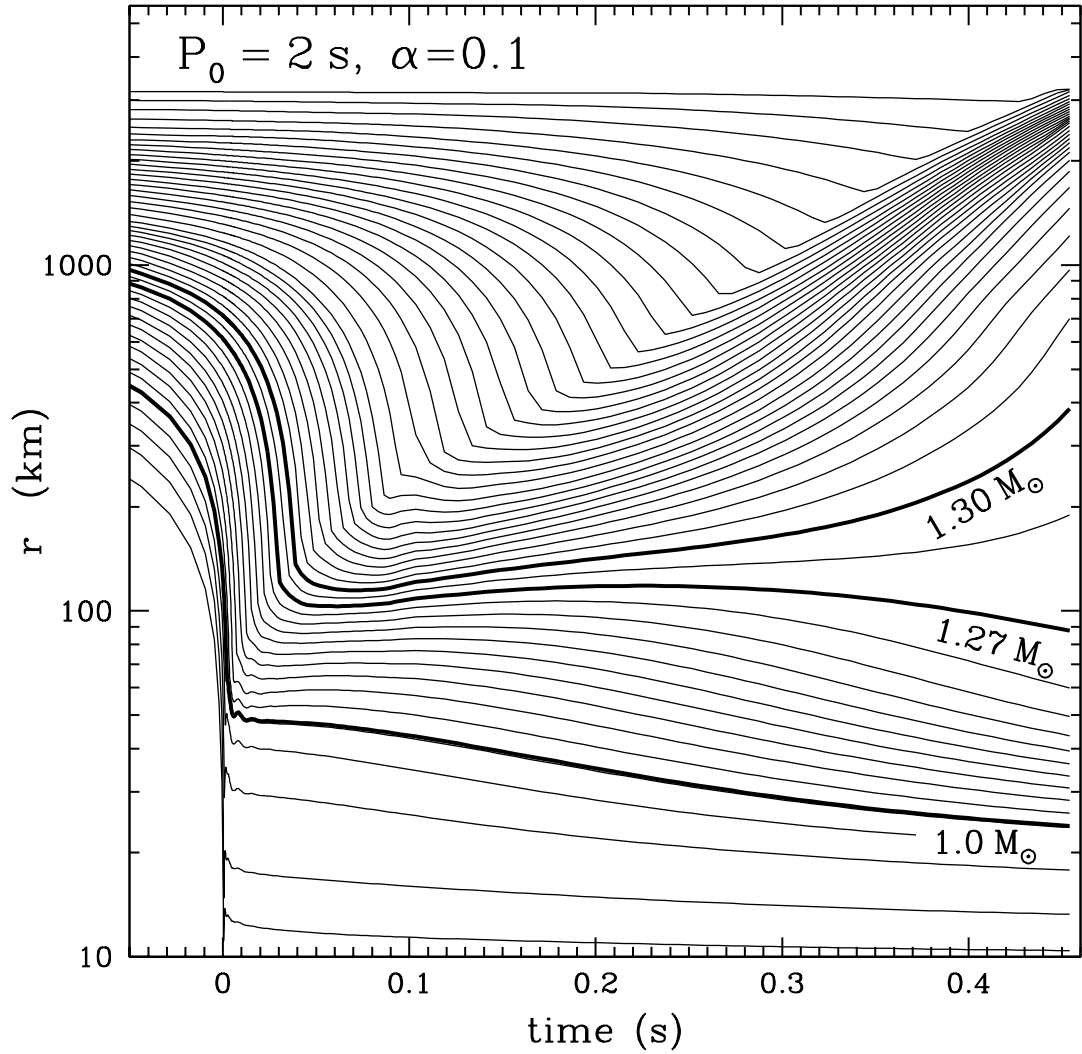


FIG. 11.— Radial position of mass elements as a function of time in a model with  $P_0 = 2$  s and  $\alpha = 0.1$ . Viscous dissipation was assumed to occur throughout the radial profile. The mass cut is initially at between  $1.27 M_\odot$  and  $1.3 M_\odot$ . Note that for clarity only every tenth mass zone is shown in this figure.

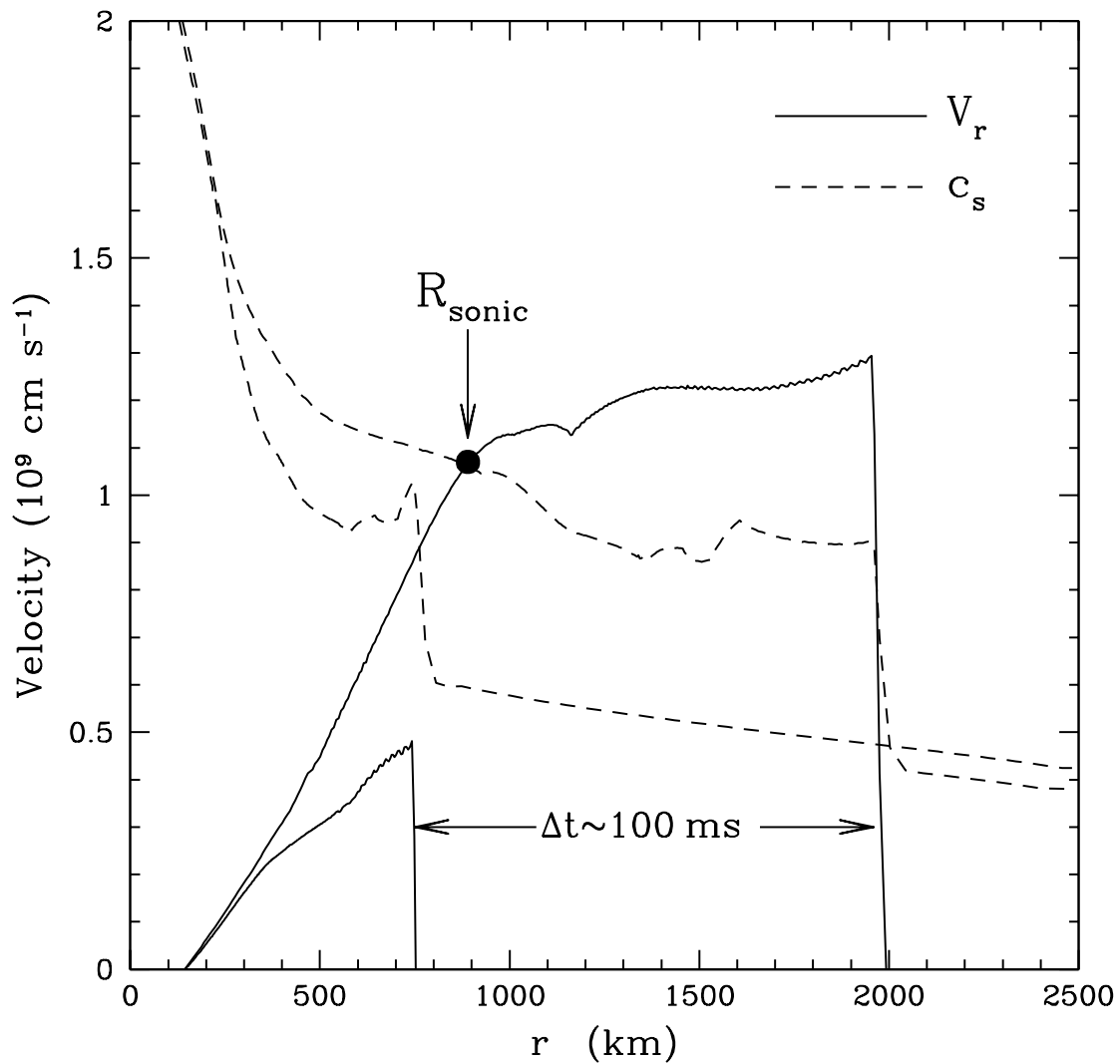


FIG. 12.—Matter velocity and adiabatic sound speed at two snapshots during explosion in the model with  $P_0 = 2$  s (Figs. 10 and Fig. 11). Note the development of the sonic point on a timescale of  $\sim 100$  ms.